3-22-2012

Electrical and Optical Characterization of Si-Ge-Sn

Merle D. Hamilton

ELECTRICAL AND OPTICAL CHARACTERIZATION OF SI-GE-SN

THESIS

Merle D. Hamilton, Captain, USAF

AFIT/APPLPHY/ENP/12-M06

DEPARTMENT OF THE AIR FORCE
AIR UNIVERSITY

AIR FORCE INSTITUTE OF TECHNOLOGY

Wright-Patterson Air Force Base, Ohio

AFIT/APPLPHY/ENP/12-M06

ELECTRICAL AND OPTICAL CHARACTERIZATION OF SI-GE-SN

THESIS

Presented to the Faculty

Department of Engineering Physics

Graduate School of Engineering and Management

Air Force Institute of Technology

Air University

Air Education and Training Command

In Partial Fulfillment of the Requirements for the

Degree of Master of Science in Applied Physics

Merle D. Hamilton, BS

Captain, USAF

March 2012

AFIT/APPLPHY/ENP/12-M06

ELECTRICAL AND OPTICAL CHARACTERIZATION OF SI-GE-SN

Merle D. Hamilton, BS

Captain, USAF

Approved:

Yung Kee Yeo Yung Kee Yeo, PhD (Chairman)	5 March 2012 Date
Robert L Hengehold Robert Hengehold, PhD (Member)	5 March 2012 Date
Nancy C. Giles Nancy C. Giles, PhD (Member)	5 March 2012 Date
 Michael Marciniak, PhD (Member)	5 Mar 12 Date

Abstract

The electrical characterization of boron-doped p-$Si_{0.08}Ge_{0.90}Sn_{0.02}$/$p$-Ge(100) and p-$Si_{0.112}Ge_{0.86}Sn_{0.028}$/$n$-Si(100) with various epilayer thicknesses was measured using the Hall effect. The room temperature sheet carrier concentration ranged from $1.21 \times 10^{13} - 1.32 \times 10^{16}$ cm^{-2}. The room temperature mobilities were measured to be between 166 and 717 $cm^2/V \cdot s$, depending on sample composition. In the low temperature regime, the mobility was mainly affected by ionized impurity scattering. In the high temperature regime, the mobility was mainly affected by both alloy and lattice scattering. The acceptor activation energy was estimated to be 10.7 meV. The Hall data indicated that an interfacial layer between the epilayer and substrate participated in both carrier concentration and hall mobility measurements. From the results of infrared transmission measurements of the p-$Si_{0.08}Ge_{0.90}Sn_{0.02}$/$p$-Ge(100) at room temperature, an effective mass was estimated to be $m_{hh} = 0.30m$, $m_{lh} = 0.051m$, $m_{so} = 0.79m$, and $\Delta\epsilon = 0.30\ eV$, where $\Delta\epsilon$ is the splitting between heavy hole and split-off valence bands. The indirect and direct bandgap energy values for the p-$Si_{0.112}Ge_{0.86}Sn_{0.028}$/$n$-Si(100) were estimated to be 0.780 eV and 0.845 eV, respectively. The results of photoluminescence measured at 15 K, for the p-$Si_{0.08}Ge_{0.90}Sn_{0.02}$/$p$-Ge(100) sample with a 600 nm film thickness, revealed the onset of a luminescence peak at 0.885 eV.

Acknowledgments

I wish to express my sincerest appreciation to my advisor, Dr. Yung Kee Yeo, for his assistance and for accepting me as a member of such an exciting and ground breaking group. I thank my other advisors, Drs. Hengehold, Giles, and Marciniak, for their ideas and recommendations.

I have met, and welcomed the assistance of many people in the course of this study. I would like to recognize the following people for their much needed assistance and advice: Drs. Kang, Ryu, and Ahoujja for their help with Hall effect measurements, sample provision and preparation; Greg Smith and Mike Ranft for their help in setting up the reflectivity measurement apparatus and advice on almost every experiment I performed, Dr. Eyink from AFRL/RX, for his assistance in spectroscopic ellipsometry; and Thomas Harris, who not only instructed me on taking photoluminescence measurements, but mentored me on many aspects of physics and the thesis process.

Finally, I would like to thank the Air Force Office of Scientific Research, Physics and Electronics Directorate for sponsoring this work.

Merle D. Hamilton

Table of Contents

Page

List of Figures

Figure Page

List of Tables

ELECTRICAL AND OPTICAL CHARACTERIZATION OF Si-Ge-Sn

Introduction

Data transfers within a microprocessor have been operating at multi-gigahertz speeds for more than a decade. Unfortunately, the copper lines used to connect microprocessors and external memories suffer signal losses of 50% at 2 GHz and an astounding 98% at 10 GHz [1]. These losses are due to resistive effects inherent in metals. The solution, which has long been adopted by the telecom industry, is signal transmission via photons. The problem with this solution, until recently, has been that integrated circuits use electrons for bit storage, transport and manipulation, making the introduction of metals a requirement in computing infrastructure. In 2007, Intel© changed this by demonstrating a 40 Gbps strained Si-Ge photodetector with only a 5% signal loss. The Si-Ge photodetector converts incoming photons into electrical signal and, because it is a Si based device, it is easily compatible with current microprocessor infrastructure. An added benefit is that the photodetector operates in the 1.3-1.6 μm telecommunication range [2].

In order to create the Si-Ge heterostructure with this type of efficiency, strain engineering had to be employed. Strain engineering can lead to several issues in making device quality structures, such as threading defects and dislocations. Ultimately, these problems can cause signal loss and device failure.

Due to recent advances in ultra-high-vacuum chemical-vapor-deposition (UHV CVD) techniques at Arizona State University, stable Ge-Sn and Si-Ge-Sn alloys have been epitaxially grown on Ge, Si, and GaAs substrates. Since Ge-Sn and Si-Ge-Sn are lattice matched [3] and have shown response in the entire telecom band [4], these all-group-IV semiconductor structures may be the best candidates to alleviate the problems of strain-engineered Si-Ge. However, further investigation is required to characterize the properties of Ge-Sn and Si-Ge-Sn and ensure it is better suited for the task of either replacing or becoming an alternative to strain-engineered devices.

The important properties to be investigated are residual impurities and their energy levels, defects, optically active transitions, bandgap energies, mobility, conductivity, and carrier concentrations in Si-Ge-Sn alloys as a function of alloy composition, sample temperature and device structure.

If Ge-Sn or Si-Ge-Sn is found to be of opto-electronic device quality, the material could revolutionize computing. This would significantly benefit Air Force and Department of Defense mission capabilities in the area of data transfer and processing. This research will be critical in furthering device creation of Si-Ge-Sn optoelectronics.

1.1 Objectives

Optoelectronic devices operating in the 1.3-1.6 μm range are a topic of intense current research. These infrared (IR) devices are of particular interest to the Department of Defense and a breakthrough in this area could significantly enhance communication mission capabilities. Si-Ge-Sn and Ge-Sn alloys are materials that have shown good preliminary optical responses in the IR telecom regime [4]. However, the optical and

electrical properties of these alloys are not well characterized yet. Therefore, systematic studies of these materials are critical for device fabrication.

The objective of this study is an investigation of the residual impurities and their energy levels, defects, optically active transitions, bandgap energies, mobilities, conductivities, and carrier concentrations in newly developed Si-Ge-Sn alloys as functions of alloy composition, sample thickness, sample temperature, and device structure. The optical characterization studies were carried out by PL, transmission, and absorbance measurements. The electrical characterization studies were made by Hall effect measurements [5].

1.2 Background

Silicon (Si) is the bedrock of our society's computing infrastructure. Germanium (Ge) is an extremely responsive optical detector. For years, researchers have been attempting to combine the two materials to make optoelectronic devices. Unfortunately, Si-Ge semiconductors have an indirect bandgap. Making direct bandgap material of Si-Ge has so far been impossible without the use of strain engineering to lower the direct bandgap, a technique that is difficult, time-consuming, and prone to defects [6].

Until recently, growth of Ge-Sn and Si-Ge-Sn has been hampered by lattice mismatches of up to 15%. In 2002, researchers in the Department of Chemistry and Biochemistry at Arizona State University created a novel method of alloying Ge-Sn on Si(100) using UHV-CVD. Si-Ge-Sn was also developed by the same group in 2003, but has been studied to a lesser extent due to the alloys' initial growth solely as a buffer layer for Ge-Sn. The most intriguing aspect of these semiconductor structures is the possibility

of creating a direct bandgap semiconductor from all group IV materials. By alloying with α-Sn, the direct gap and indirect gap energies of Ge are both reduced. The direct gap reduces faster with additional Sn, making bandgap tuning possible. Currently, only 0.06 percent Sn is required to convert the Ge-Sn alloy to a direct gap semiconductor [7]. Additionally, these structures have a root mean squared surface roughness of 0.5-1.4 nm, which is comparable to Si [8]. The growth temperature ranges from 250-350 °C and the Si-Ge-Sn semiconductor structures have shown stability at temperatures greater than 800 °C [9].

1.3 Semiconductors

There are three important topics to understand when investigating semiconductors. First is the band structure, next is the distribution function of the charge carriers, and finally the density of states. These three fundamental processes can give great insight into Hall effect, transmission, absorbance, and PL experiments.

1.3.1 Band Structure

The full derivation of a semiconductor's band structure involves a complete quantum mechanical treatment where each wave function extends throughout the entire lattice [10, 11]. This is an extremely complex problem. The tight binding approximation, coupled with Bloch's theorem, essentially reduces the wave function overlap to nearest neighbors thus simplifying the derivation greatly. Let $H_{at}\psi_j = E_j\psi_j$ where H_{at} is the crystal's Hamiltonian and ψ_j is the Bloch function of the j^{th} electron, given by $\psi_{j,k}(r+T) = Ce^{ikT}\psi(r)$, where C is a normalization constant depending on the number of atoms in the lattice, $C = N^{-1/2}$, and T is a translation of the direct lattice. H_{at}, is given by:

$$H = \frac{p^2}{2m} + \sum_j V(r - R_j), \tag{0.1}$$

where V is the atomic potentials centered at the various sites, j, in the lattice. When $j = j'$, the Hamiltonian will be large compared to the other values considering that atomic potentials decrease rapidly with distance. Let $\frac{p^2}{2m} + V(r - R_j) = H_0$. Thus, $H_{at}\psi_{j,k} = E_0\psi_{j,k} + \sum_{j\neq j'} V(r - R_{j'})\,\psi_{j,k}$. Multiplying by $\psi^*_{j,k}$ and integrating:

$$E = < \psi_{j,k}^{*} | E_0 | \psi_{j,k} > + \int \psi_{j,k}^{*} \sum_{j \neq j'} V(r - R_{j'})\, \psi_{j,k} dr^3, \tag{2.2}$$

and further separating equation (2.2) into nearest neighbor and next-nearest neighbor terms

$$E = E_0 + \int \psi_{j,k}^{*}\, V(r - R_{j'}) \psi_{j,k} dr^3 \; + \int \psi_{j,k}^{*} \sum_{j \neq j' \neq j''} V(r - R_{j'})\, \psi_{j,k} dr^3. \tag{2.3}$$

Call the first integral $-\alpha$ and let

$$\int \psi_{j,k}^{*} \sum_{j \neq j' \neq j''} V(r - R_{j'})\, \psi_{j,k} dr^3 \; = \; -\gamma \sum_{j \neq j' \neq j''} e^{ik\left(R_j - R_{j'}\right)}. \tag{2.4}$$

We conclude that

$$E = E_0 - \alpha - \gamma \textstyle\sum_{j \neq j' \neq j''} e^{ik\left(R_j - R_{j'}\right)}, \tag{2.5}$$

with the last term giving rise to bands. As an example, Leman [12] performed this calculation for a face centered cubic crystal and an electron configuration of column IV atoms, ns^2np^2. The hybrid s and p eigen states are $\phi_{0,1} = \frac{\phi_s \pm \phi_x \pm \phi_y + \phi_z}{2}$ and $\phi_{2,3} = \frac{\phi_s \mp \phi_x \pm \phi_y - \phi_z}{2}$ with eigenvalues of $< \phi_j | H_0 | \phi_j > = \frac{1}{2}(E_s + 3E_p)$ and $< \phi_j | H_0 | \phi_{j'} > = \frac{1}{4}(E_s - E_p)$. This results in 6 bands with the energy gap equal to $E_g = 2E_c - 5\ (eV)$, where E_c is the binding energy (or cohesive energy) as shown in figure 1. Experimentally, one observes $E_g = 1.85E_c - 5.36\ (eV)$, demonstrating the agreement with this approximation. Figure 1 gives a benchmark for the expected energy values that one expects to observe for Si-Ge-Sn alloys.

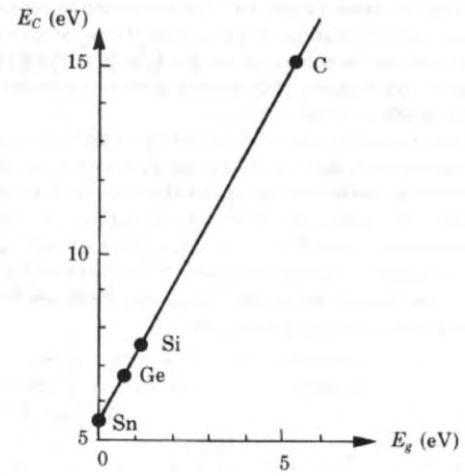

Figure 1. The relation between cohesive energy and bandgap width obtained by LCAO method for the sequence of crystals of elements of column IV of the Periodic Table [11].

1.3.2 Density of States

The density of states can be thought of as the number of states per unit volume in a certain energy range. In momentum space, if a spherical energy surface with constant energies of $\epsilon + d\epsilon$ is assumed, one can describe this surface as $p_x^2 + p_y^2 + p_z^2 = 2m^*\epsilon$, where p_x, p_y, and p_z are momentum values in the *x*, *y*, and *z* directions, respectively, and m^* is the electron effective mass. The volume of the surface is $dV_p = 4\pi p^2 dp$. Combining these two equations, $dV_p = 4\pi m^* \sqrt{(2m^*\epsilon)} d\epsilon$. The density of states can then be described by $\frac{dV_p}{V_p} = \frac{4\pi m^* \sqrt{2m^*\epsilon}}{h^3/2V} d\epsilon$ or finally $g(\epsilon)d\epsilon = \frac{8\sqrt{2}\pi V m^{*\frac{3}{2}}\sqrt{\epsilon}}{h^3}\, d\epsilon$. In two dimensions, instead of using dV_p, the change in area, A_p, is used. Here, $dA_p = 2\pi m^* d\epsilon$ and following the same method as above, $g(\epsilon)d\epsilon = \frac{4\pi m^* A}{h^2}\, d\epsilon$. The density of states in one dimension is $g(\epsilon)d\epsilon = \frac{1}{h}\sqrt{\frac{2m^*}{\epsilon}} d\epsilon$, as shown in figure 2. The density of states of a material can be observed in band-to-band transitions on the low energy side of both

luminescence and absorption experiments; it is also key in Hall effect measurement analysis.

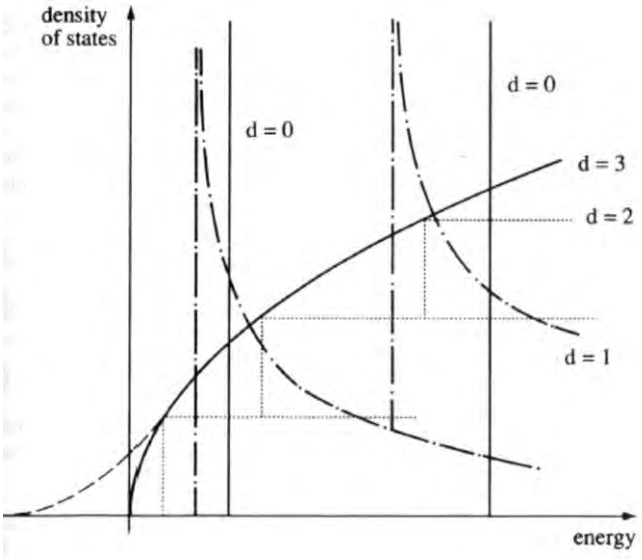

Figure 2. Schematic drawing of the density of states as a function of energy for three-, and quasi-two-, one- and zero-dimensional systems in the effective mass approximation. The dashed line corresponds to disorder-induced localized states [13].

1.3.3 Distribution of Charged Carriers

In thermal equilibrium, t he distribution of electrons in a semiconductor can be described by the Fermi Dirac distribution function:

$$f_e(E) = \frac{1}{e^{\frac{E-E_f}{kT}}+1}, \tag{0.6}$$

where k is Boltzmann's constant, T is temperature, and E_f is the Fermi level, located in the middle of the bandgap for intrinsic semiconductors at 0 K. For holes, $f_h(E) = 1 - f_e(E)$. When the density of states, $g(\epsilon)$, is multiplied by the distribution function and integrated, one can determine the concentration of charge carriers:

$$N(\epsilon)d\epsilon = f(\epsilon)g(\epsilon)d\epsilon. \quad (0.7)$$

For p-doped semiconductors the distribution of charge carriers differs from (2.6). Let N_a be a concentration of acceptors in the material. At temperatures where the Fermi energy level is above the acceptor energy level, the acceptor level will be populated with electrons, creating holes in the valence band. This shifts the Fermi energy level to $E_f = kTln\left(\frac{N_v}{N_a}\right) + E_v$, where k is Boltzmann's constant, T is the temperature, N_v is the concentration of holes in the valence band, and E_v is the energy of the valence band as shown in figure 3.

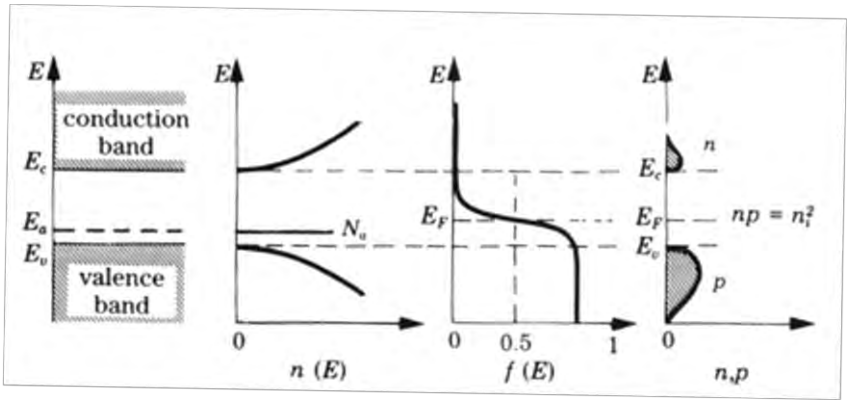

Figure 3. From left to right, the band diagram, the density of states, the Fermi function and the carrier concentration as a function of energy for a *p*-type semiconductor at room temperature [11].

1.4 Photoluminescence

The purpose of this section is to inform the reader on band-to-band processes that can be attributed to the various structures observed in PL. PL is a non-invasive and fairly straightforward method of interrogating excitonic and defect states in semiconductors. PL can also be used to determine band-to-band transitions in a semiconductor, although reabsorption above bandgap energy can make this technique more difficult.

In a direct gap material, as shown in figure 4a, a photon with energy greater than the bandgap is absorbed by the material causing an electron-hole pair to be created. The electron-hole pair undergoes a non-radiative transition from level 5 to 4, figure 4b, and then may recombine, emitting a photon of longer wavelength. In general, state 4 can recombine into three different states, the light hole (lh) band, heavy hole (hh) band and split-off (so) band, however, the direct, or gamma point, transition is the most probable.

In an indirect gap material, depicted in figure 4c, this transition process is different. The electron-hole pair still undergoes a non-radiative transition from 6 to 5 (figure 4d), but in order for a radiative transition to occur (5→3, 5→2, 5→1), at least one phonon must be either absorbed or emitted simultaneously (5→4) to conserve momentum, thus making luminescence in indirect gap material much less likely than direct gap material. To illustrate this point, it has been shown that the recombination rate is related to $B_{direct} \sim 10^{-8} cm^3 s^{-1}$ and $B_{indirect} \sim 10^{-15} cm^3 s^{-1}$ for the indirect gap of Ge [14]. For PL of Ge, this may seem counter-intuitive because the luminescence from the indirect gap is more intense, but because the population of charge carriers in the direct gap is much less than that in the indirect gap, the luminescence is still greater from the indirect gap.

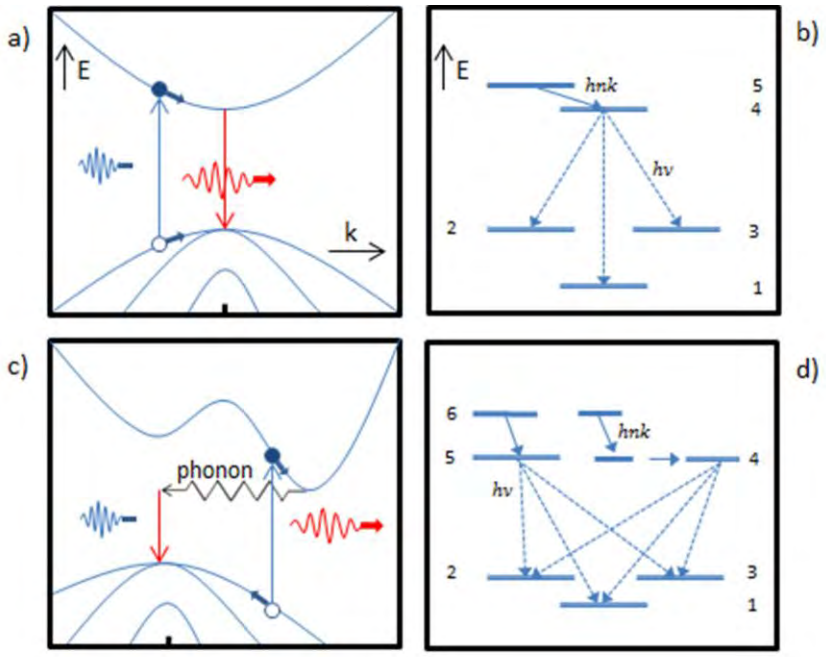

Figure 4. Left (a,c), band representation in momentum space of a direct and indirect gap semiconductor, respectively. Right (b,d), energy diagram for radiative (dashed arrows) and non-radiative (solid arrows) recombination in a direct and indirect gap semiconductor.

Acc ording to Pankove [15], the most probable simultaneous transition is emission of a phonon. The number of phonons available for absorption is small and rapidly decreases with decreasing temperature. Thus, at lower temperatures one would expect a more intense PL signal as less energy is used for excitation of phonons not participating in radiative recombination. Phonons have six possible modes, two of transverse acoustic, two of transverse optical, and one mode each of longitudinal acoustic and optical. Multiple phonon emission and absorption is also possible but with less probability. The average phonon energy is related to the Debye temperature, Θ, of a material by $\epsilon_{av} = \frac{2}{3}k\Theta$ where k is Boltzmann's constant. For Ge, the Debye temperature is 378 K making the average phonon energy 21 meV.

The intensity of band-to-band luminescence is given by the equation

$$I \sim |M|^2 g(h\nu) N(h\nu), \tag{0.8}$$

where $|M|^2$ is the quantum mechanical transition probability, and $g(h\nu)$ and $N(h\nu)$ are the density of states and concentration of charge carriers respectively. A direct gap material with a low enough concentration of charge carriers, which can be used for the Maxwell Boltzmann approximation for the distribution function has a luminescence line shape shown below with proportionality constant *C,* temperature *T,* and Boltzmann's constant *k*:

$$I = C\left(\epsilon - \epsilon_g\right)^{1/2} e^{-\frac{\epsilon - \epsilon_g}{kT}}. \tag{0.9}$$

Solving for ϵ_g, the bandgap energy, is straight forward by taking the derivative of equation (2.9) and setting it equal to zero. This results in the luminescence peak, $\epsilon_{peak} = \epsilon_g + \frac{kT}{2}$. For a degenerate semiconductor, equation (2.9) is slightly more difficult considering that the Maxwell Boltzmann approximation cannot be used. In this case, $\epsilon_{fermi}^{c,v} = \frac{\hbar^2}{2m_{e,h}^*}\left(3\pi^2 N_{e,h}\right)^{\frac{2}{3}}$, where *c* or *v* represents the conduction or valence band, respectively, and $N_{e,h}$ is the carrier concentration of electrons or holes, respectively. Additionally, when self-absorption affects are considered the intensity of luminescence, equation (2.9), changes. If the radiative recombination occurs uniformly inside the sample, the emitted intensity, I_{se}, is given by,

$$I_{se} = \frac{(1-R)I(1-e^{-\alpha t})}{\alpha t}, \tag{0.10}$$

where R is the reflectance of the exit surface, I is the emission spectrum given by equation (2.9), α is the absorption coefficient (discussed in more detail below), and t is

the thickness of the sample. From equation (2.10), it is apparent that the emission spectrum will be reduced significantly for samples that are strongly absorbing [15].

Excitonic radiation can be from either free exciton or bound exciton transitions. Free excitons can be thought of as free carrier pairs that have hydrogen-like interaction in the lattice. Free excitons usually extend over large distances in the lattice and the emission can be identified by a high energy luminescence peak. The intensity of free exciton luminescence is described mathematically by

$$I = Ce^{-\frac{\epsilon-\epsilon_x}{kT}}e^{-\frac{(\epsilon-\epsilon_x)^2}{2\sigma^2}}, \tag{0.11}$$

where ϵ_x is the free exciton energy and σ is related to the full width at half max by $FWHM = 2\sigma\sqrt{2ln2}$. On the other hand, bound excitons, which stem from impurity centers in the lattice, can be identified on the low energy side of the free exciton luminescence peak. Bound excitons have a full width at half maximum on the order of meV. Often bound and free excitons will be observed together [15].

Impurities, vacancies, dislocations, and boundaries can also lead to other forms of radiative recombination. Impurities are most easily thought of as a hydrogen-like system. With increasing temperature, the impurity atom ionizes causing an attractive force on conduction band electrons and repulsive force on valence band holes. In a *p*-type material, such as boron doped Si-Ge-Sn, impurities create a tailing in the density of states in the valence band. This leads to lower energy tailing as temperature increases.

Band-to-band recombination in *p*-type material should show power dependence in luminescence considering that there are more majority carriers (holes) than minority

carriers (electrons). As incident power is increased, more minority carriers are created thus intensity should have a nearly linearly proportionality to excitation energy [16].

1.5 Transmission of Light through a Material

Much can be learned by the transmission of light through a semiconductor. The simplest case is transmission through a uniform material. *T*, the ratio of transmitted power over incident power, is equal to incident intensity multiplied by the amount not reflected on the first surface, R_1, and by the amount absorbed by the material and by the reflected light as the light exits the material, R_2: $T = (1 - R_1)e^{-\alpha t}(1 - R_2)$, where *t* is the thickness of the material, and α is the absorption coefficient. If the material is in a uniform environment where $R_1 = R_2$, then $T = (1 - R)^2 e^{-\alpha t}$. When multiple reflections at the surfaces of the material are considered, the resulting transmission can be described by: $T = \frac{(1-R^2)e^{-\alpha t}}{1-R^2 e^{-2\alpha t}}$. The reflectivity R at normal incidence is given by: $R = \left(\frac{\tilde{n}_2 - \tilde{n}_1}{\tilde{n}_2 + \tilde{n}_1}\right)^2$, where $\tilde{n}_2$and $\tilde{n}_1$ are the complex indices of refraction for the material and the ambient environment, respectively. The absorption coefficient α, for an indirect gap semiconductor, is proportional to $\alpha \sim \left(E - E_g\right)^2$ and for a direct gap semiconductor, $\alpha \sim \left(E - E_g\right)^{1/2}$. In thin films, sometimes the absorption of the substrate cannot be decoupled from that of the epilayer and thus the absorbance, in units of optical density (OD), is used in place of the absorption coefficient. The absorbance, $A = -Log_{10}(T)$.

For *p*-type semiconductors, transitions are possible between the lh, hh, and so bands [15]. This appears to be first theoretically studied by Khan [17] for Ge and Si. The absorption coefficient for the first and second valence bands (hh and lh) is

$$\alpha_{12}(\epsilon) = C\sum_{k_1,k_2}\langle|M_{12}|^2\rangle(f_1 - f_2)\delta(\epsilon_2 - \epsilon_1 + \epsilon)\delta_{k_1,k_2}, \tag{2.12}$$

where $\alpha_{1,2}$ is the absorption coefficient for the lh-hh transition, but more generally, $\alpha_{i,j}$ is the absorption coefficient for transitions between the *j* and *i* bands where 1, 2, and 3 are the hh, lh, and so bands, respectively. In equation (2.12), M is the interband transition matrix mentioned previously, *C* is a constant, ϵ_i is the spherical energy surface approximation for the i[th] band, δ_{k_1,k_2} is the Kronecker delta, and $\delta(\epsilon_2 - \epsilon_1 + \epsilon)$ is a delta function. A further approximation to equation (2.12) is the use of a Maxwell Boltzmann distribution, given by $f_i(\vec{k}) = \frac{N_i\hbar^3}{(2\pi m_i^* kT)^{\frac{3}{2}}}e^{-\frac{E_i}{kT}}$, where N_i, which is the number of carriers in the i^{th} band, m_i^* is the effective mass of the band, k is Boltzmann's constant, T is the temperature, $\hbar$ is Planck's constant divided by 2π, and E_i is the energy. When equation (2.12) is solved for the transitions within the three bands, one obtains the following equations:

$$\alpha_{lh-hh}(\epsilon) = \frac{16\pi^2\sqrt{2}e^2\hbar^{\frac{3}{2}}A_{1,2}^2 m_1^* m_2^{*\frac{5}{2}}N\sqrt{\frac{\epsilon}{hc}}}{nc^{\frac{1}{2}}\left(1 + \left(\frac{m_2^*}{m_1^*}\right)^{\frac{3}{2}}\right)m^2(m_1^* - m_2^*)^{\frac{5}{2}}(kT)^{\frac{3}{2}}} * \tag{0.13}$$

$$\left[\exp\left(-\frac{\epsilon * m_2^*}{kT(m_1^* - m_2^*)}\right) - \exp\left(-\frac{\epsilon * m_1^*}{kT(m_1^* - m_2^*)}\right)\right],$$

$$\alpha_{so-hh}(\epsilon) = \frac{16\pi^2\sqrt{2}e^2\hbar^{\frac{3}{2}}A_{1,3}^2 m_1^* m_3^{*\frac{5}{2}}N\left(\frac{\epsilon}{hc} - \frac{\Delta\epsilon}{hc}\right)^{\frac{3}{2}}}{nc^{\frac{1}{2}}\left(1 + \left(\frac{m_2^*}{m_1^*}\right)^{\frac{3}{2}}\right)m^2(m_1^* - m_3^*)^{\frac{5}{2}}\frac{\epsilon}{hc}(kT)^{\frac{3}{2}}} * \tag{0.14}$$

$$\exp\left(-\frac{(\epsilon-\Delta\epsilon)m_3^*}{kT(m_1^*-m_3^*)}\right),$$

and

$$\alpha_{so-hh}(\epsilon)=\frac{16\pi^2\sqrt{2}e^2\hbar^{\frac{3}{2}}A_{2,3}^2\,(m_2^*/m_1^*)^{\frac{3}{2}}m_2^*m_3^{*\frac{5}{2}}N\left(\frac{\Delta\epsilon}{hc}-\frac{\epsilon}{hc}\right)^{\frac{3}{2}}}{nc^{\frac{1}{2}}\left(1+\left(\frac{m_2^*}{m_1^*}\right)^{\frac{3}{2}}\right)m^2(m_3^*-m_2^*)^{\frac{5}{2}}\frac{\epsilon}{hc}(kT)^{\frac{3}{2}}}* \tag{0.15}$$

$$\exp\left(\frac{(\epsilon-\Delta\epsilon)m_3^*}{kT(m_3^*-m_2^*)}\right).$$

In equations (2.13)-(2.15), N is the concentration of charge carriers; m_1, m_2, and m_3 are the effective masses of the hh, lh, and so bands, respectively; n is the index of refraction; $\Delta\epsilon$ is the energy difference between the hh and so bands; and $A_{i,j}$ is a dimensionless parameter. For a full quantum mechanical treatment, see Basu [18] or Khan [17]. It is straight forward to show that the maximum in absorption occurs at $\epsilon_{1,3}=\Delta\epsilon+\frac{3}{2}kT\frac{(m_1^*-m_3^*)}{m_3^*}$ and $\epsilon_{2,3}=\frac{1}{4m_3^*}(kT(m_2^*-m_3^*)+2m_3^*\Delta\epsilon+\sqrt{16kT(m_2^*-m_3^*)m_3^*\Delta\epsilon+(kT(m_2^*-m_3^*)+2m_3^*\Delta\epsilon)^2})$. To solidify the matter, figure 5 shows the corresponding valence band transitions for p-Ge with $m_1^*=0.3m$, $m_2^*=0.04m$, $m_3^*=0.095m$ and $\Delta\epsilon=0.29\ eV$. Figure 5 is an example of equations (2.13)-(2.15) for Ge, as well as the addition of the Urbach tail, discussed below.

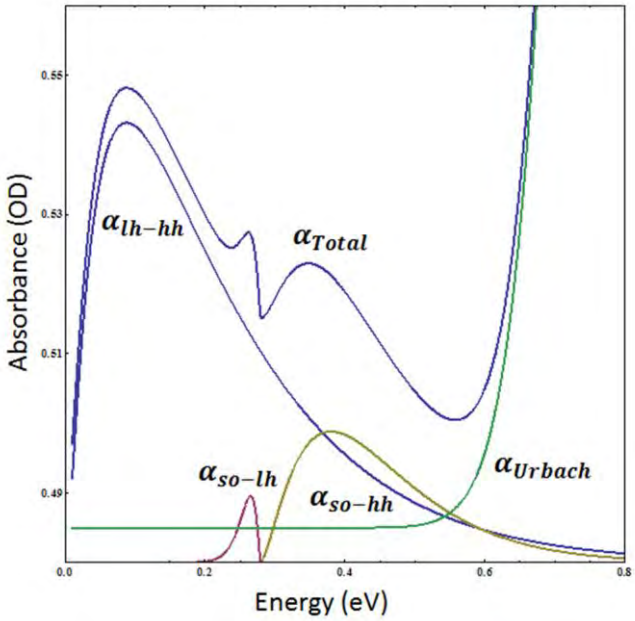

Figure 5. A theoretical interband absorbance curve for *p*-Ge at room temperature. α_{Total} is the summation of the absorption from the lh-hh, so-lh, so-hh, and the Urbach tail for Ge.

1.5.1 Urbach Tails

Urbach tails can be identified by an exponential increase of absorption below the direct band edge of a semiconductor. The source of this absorption can have different origins, including local dipole fields due to phonons, local strain fields due to dislocations, and fields due to coulombic interactions between charge impurities. Identification of the major contributing source of this absorption can be done by analyzing the temperature dependence of the absorption in the following way. Let

$$\alpha_{Urbach} = \alpha_o e^{\frac{\sigma(\hbar\omega - E_0)}{kT}}, \tag{0.16}$$

where α_o and E_0 are characteristic parameters of the matieral [19], σ is a steepness parameter, k is the Boltzmann constant, T is the temperature, and $\hbar\omega$ is the energy. Equation (2.16) can be further simplified to

$$\alpha_{Urbach} = \alpha_o e^{\frac{(\hbar\omega - E_0)}{E_w}}, \tag{0.17}$$

where E_w is called the energy broadening. For most materials, E_w is the sum of two terms, one dependent on temperature and one independent of temperature. The term independent of temperature is related to the disorder in the material and the term that is dependent of temperature can be related to the average phonon energy, $\hbar\omega_{phonon}$, by $\sigma = \sigma_o \frac{2kT}{\hbar\omega_{phonon}} \tanh(\frac{\hbar\omega_{phonon}}{2kT})$, where σ_o is a parameter dependent on the material.

1.5.2 Free Carrier Absorption

Free carrier absorption is different from intervalence band absorption, which was described above. However, there are some similiarities. For example, free carrier absorption is observed below the band edge of the material. These effects are most noticable between 5-30 μm [20]. The primary difference between the two is that free carrier absorption occurs from an electron being excited by a photon above the Fermi energy level in the same band, as shown by the black arrow in figure 6. This effect can be observed in both *n* and *p*-type semiconductors and the absorption, $\alpha_{free\ carrier}$ is related to *N*, the carrier concentration of free electrons or holes generated by the doping process, *q* the magnitude of the charge of the electron, *m**, the effective mass of either the electron or hole, *n* the index of refraction, *c*, the speed of light, τ, the damping time, the permitivity of free space, and the radial frequency of light ω by:

$$\alpha_{free\ carrier} = \frac{Nq^2}{m^*\epsilon_0 nc\tau}\frac{1}{\omega^\beta}, \tag{0.18}$$

where β ranges from 2-3 [20]. For *p*-type semiconductors, optical transitions can take place between the different bands within the valence, as depicted by red arrows in figure

6, specifically transitions are made between the so-lh bands, so-hh bands, and lh-hh bands. Both free carrier and intervalence band absorption are depicted in figure 6 for clarification.

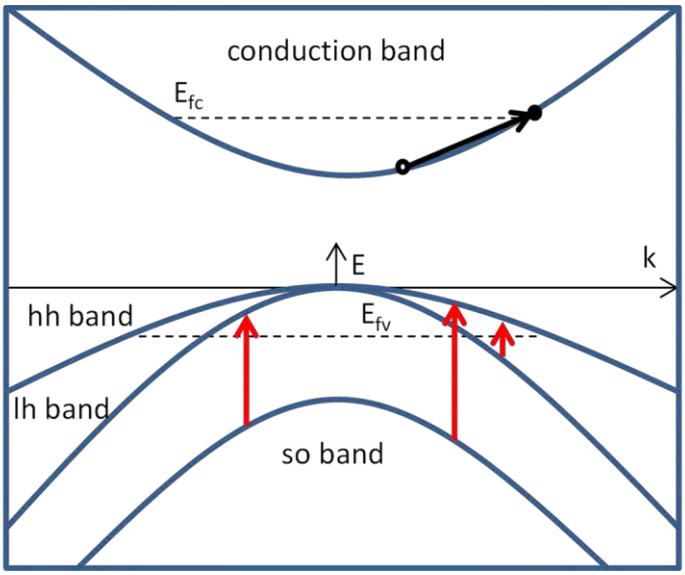

Figure 6. A graph of the valence and conduction bands in a direct gap semiconductor, depicting the difference between free carrier and intervalence band absorption. Free carrier absorption, black arrow, is depicted in the conduction band, where an electron is optically excited above the quasi-Fermi level in the same band. Intervalence band absorption, red arrows, are depicted in the valence band where electrons are optically excited above the quasi-Fermi level to different bands.

1.6 Hall Effect

1.6.1 Overview

The Hall effect measures both resistivity and Hall voltage of a semiconductor at varying temperatures in a magnetic field. From these two measurements, analyses of carrier concentration, conduction type, and mobility can be made.

When a magnetic field is applied to a current carrying sheet, carrier drift occurs. This drift, caused by the Lorentz force, results in a net potential difference across the bulk

of the material. For the van der Pauw technique, depicted in figure 7, the two measured resistances R_A and R_B are related through the van der Pauw equation: $e^{-\frac{\pi R_A}{R_S}} + e^{-\frac{\pi R_B}{R_S}} = 1$. Here, the bulk resistivity ρ, is related to the sheet resistance R_S by the equation $\rho = R_S d$, where d is the thickness of the sample. For epitaxially grown films, this picture may change. With a *p*-*i*-*n* or *n*-*i*-*p* semiconductor sample, only the surface resistance will be measured, assuming the ohmic contacts are only on the surface. For *p*-on-*p* or *n*-on-*n* semiconductors, one can expect the substrate layer to affect the Hall measurement of the epilayer. Because it is impossible to decouple the epilayer and substrate in these scenarios care must be taken to account for the effect of the substrate. Usually the best way to remove these affects is to avoid the same conductivity type for the epilayer and substrate. In some cases, the measured carrier concentration and mobility are significantly affected by an interfacial layer that forms to relieve strain at the substrate and epitaxial layer interface [21]. The influence on Hall measurements of this interfacial layer shall be addressed below.

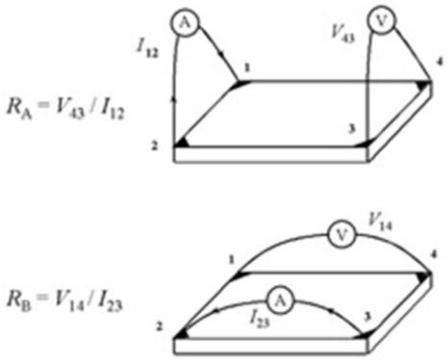

Figure 7. The van der Pauw technique, displaying how the Hall voltage is measured [22].

When the Hall voltage, V_H, is measured and the current and magnetic field are known, one can determine the Hall coefficient of the material as well as the conductivity from the equation given by:

$$R_H = \frac{E_y}{J_x B}, \tag{0.19}$$

where $J_x = \sigma E_x$. The Hall coefficient also has the form of

$$R_H = \frac{p_0 - n_o b^2}{q(n_0 b + p_0)^2} \tag{0.20}$$

in a moderate magnetic field. Here, q is the magnitude of charge on the electron, $b = \frac{\mu_n}{\mu_p}$, where μ_n is the electron mobility and μ_p is the hole mobility, and p_0 and n_o are the concentration of holes and electrons respectively. If the sample is strongly extrinsic, the Hall coefficient can be approximated as

$$R_H = \frac{1}{q' n}, \tag{0.21}$$

where q' is the charge of the dominant carrier and n is the dominant carrier concentration.

1.6.2 Conductivity

The conductivity can be described generally by $\sigma = q(n_0\mu_n + p_0\mu_p)$, where q is the magnitude of the charge of the electron, n_0 and p_0, are the carrier concentrations of the electrons and holes, respectively, and μ_n and μ_p are their mobilities. In the intrinsic regime at higher temperatures: $\sigma_i = q(\mu_n + \mu_p)n_i$, where $n_i = Ce^{-\frac{E_g}{2kT}}$. Now, at lower temperatures of the extrinsic regime for partially compensated semiconductors, where there is partial ionization of acceptors: (in p-type material) $n_i = p_0 = \left(\frac{N_v N_a}{2}\right)^{1/2} e^{\frac{-(E_v - E_a)}{kT}}$ [11]. The natural log of the carrier concentration is depicted in figure

8 for a partially compensated semiconductor. The conductivity, for extrinsic p-type material, is given by $\sigma_e = q\mu_p(N_a - N_d)$, where N_a and N_d are the concentration of acceptors and donors, respectively. For highly extrinsic material where acceptors dominat e, the conductivity can be approximated by $\sigma_e = q\mu_p p_0$.

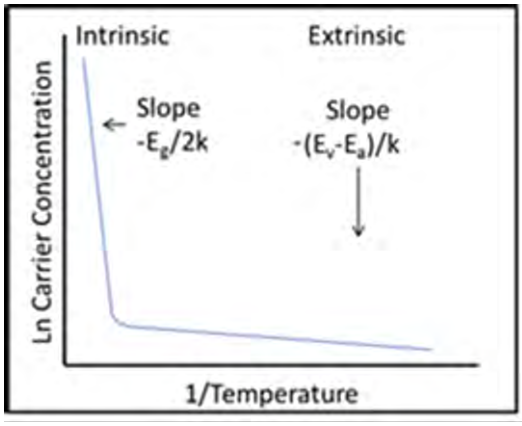

Figure 8. The natural log of the carrier concentration as a function of inverse temperature. The band edge and acceptor activation energy can be calculated from the slopes in the intrinsic and extrinsic regimes.

Ideally, a measurement of the conductivity can be used to determine both the acceptor activation energy and band edge of a *p*-type material as shown in figure 9. At low temperatures, it is possible to freeze electrons and holes onto impurity atoms. For Si and Ge, this happens below 77K [23]. This is the physical process which makes the calculation of acceptor activation energy possible.

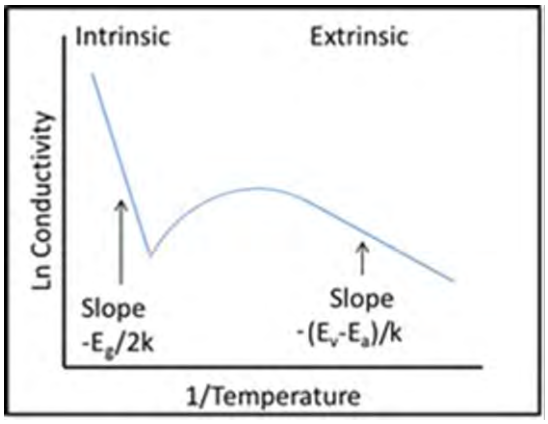

Figure 9. Natural log of conductivity as a function of inverse temperature. The band edge can be calculated from the slope in the intrinsic regime and the acceptor activation energy can be calculated from the slope in the extrinsic regime.

1.6.3 Mobility

Mobility of charge carriers, μ, gives insight into the scattering mechanisms in the material. Each scattering mechanism has a dependence on temperature; by relating the temperature dependence and the measured mobility, it is possible to model the materials transport properties.

The mobility of a material is typically derived from $\sigma = q(n_0\mu_n + p_0\mu_p)$, and for *p*-type material, it is approximated by $\sigma_e = q\mu_p p_0$, which is the equation used in the Hall effect measurement. Conductivity mobility, μ, is defined as the drift velocity per unit field or $\mu = \frac{q\tau}{m}$, where $\tau = \frac{\lambda}{3}\sqrt{\frac{8m}{\pi kT}}$ and λ is the mean free path, k is Boltzmann's constant, m is the carrier effective mass, and T is the temperature. Several scattering processes may occur in a semiconductor. Thus, in order to combine the scattering processes, one uses Matthiessen's rule: $\frac{1}{\mu} = \frac{1}{\mu_1} + \frac{1}{\mu_2} + \frac{1}{\mu_3} \ldots$.

Alloy scattering occurs when a charge carrier enters the potential of a different atom. This phenomenon is similar to that of a quantum well, and a full quantum mechanical treatment of an alloy can give very accurate predictions of temperature dependence of alloy scattering. The generic temperature dependence of alloy scattering used is $\mu \sim T^{-\frac{1}{2}}$.

Ionized impurity scattering, on the other hand, has a dependence of $\mu \sim T^{\frac{3}{2}}$ and generally arises from charge carriers scattering off dopants. Because as $T \to 0$ the mobility will approach 0, a constant, a is introduced which will allow the mobility to stay above zero, and a proportionality factor b such that $\mu \sim a + bT^{\frac{3}{2}}$ [24].

Lattice scattering occurs from the charged carrier interaction with phonons and deformations in the lattice. At lower temperatures, the lattice scattering mechanism is negligible but dominates at higher temperatures. The experimentally observed relation between temperature and mobility due to lattice scattering for p-Ge is $\mu \sim T^{-2.3}$ [23]. Theoretically for acoustical phonons, in p-type material the mobility of the holes is given by, $\mu_p = \frac{4q\lambda_p}{3\sqrt{2\pi m_p^* kT}}$, where q is the magnitude of charge of the electron, m_p^* is the hole effective mass, k is Boltzmann's constant, T is the temperature, and λ_p is the mean free path. The mean free path for acoustical phonons is inversely proportional to the density of phonons, $\frac{9NT}{2V\Theta}$, where $\frac{N}{V}$ is the number of lattice atoms per unit volume, T is the temperature , and Θ is the Debye temperature of the material. This gives theoretical temperature dependence for acoustical phonon scattering of $\mu \sim T^{-3/2}$. The theoretical temperature dependence for optical phonon scattering is $\mu \sim T^{-1/2}$. However, when one

considers the true inelastic scattering of optical phonons the temperature dependence is not analytical [21].

1.6.4 Interfacial Layer Effects on Hall Measurements

When a material is grown on similar type material, both the mobility and carrier concentrations can be artificially increased for temperatures below 400 K. This increase can stem from a large lattice mismatch, (14% in one study), between the epilayer and substrate, where a thin highly dislocated region is generated at the interface. This effect can be identified by an unexpected increase of carrier concentration and mobility in the low temperature regime. Also, in a *p*-type material, the fitted shallow donor energy will be too low and often a second deeper donor appears [21]. To correct for this effect, a multilayer analysis must be performed. The two relations that must be considered in these cases are

$$\sigma_s = \sum_i \sigma_{s,i}, \tag{0.22}$$

$$\mu_{Hs}\sigma_s = \sum_i \mu_{Hs,i}\sigma_{s,i}, \tag{0.23}$$

where σ_s is the conductivity of the entire sheet, μ_{Hs} is the conductivity mobility of the sheet, and i is the layer. For example, in a two layer system, to solve for the bulk parameters, where the bulk is $i = 1$ and the interfacial layer is $i = 2$, the following equations must be used:

$$\mu_{H,1} = \frac{\mu_H^2 n_H - \frac{\mu_2^2 n_{s,2}}{d}}{\mu_H n_H - \frac{\mu_2 n_{s,2}}{d}}, \tag{0.24}$$

$$n_{H,1} = \frac{\left(\mu_H n_H - \frac{\mu_2 n_{s,2}}{d}\right)^2}{\mu_H^2 n_H - \frac{\mu_2^2 n_{s,2}}{d}}, \tag{0.25}$$

where n_H is the uncorrected sheet carrier concentration, d is the thickness of the non-interfacial layer, and $n_{s,2}$ is the carrier concentration in the interfacial layer. For a partially compensated *p*-type semiconductor, the carrier concentration of the interfacial layer can be estimated by the donor concentration (in cm^{-2}) at the low temperature limit, the size of the interfacial layer, has been estimated to be on the order of 200 nm [21]. μ_2 can be obtained from the low temperature limit of the Hall mobility. Once $n_{H,1}$ and $\mu_{H,1}$ are obtained, they can be multiplied with the magnitude of the charge of the electron and the corrected value of the acceptor level can be estimated.

1.7 Properties of Si-Ge-Sn

A group at Arizona State University, led by J. Kouvetakis, created novel hydride precursors for use in UHV-CVD, enabling growth of $Si_xGe_{1-x-y}Sn_y$ (y = 2 - 12%) with random diamond cubic structures. A molar ratio close to 4:1 of Si to Sn gives a fixed lattice constant identical to Ge, as shown in figure 10 as the white dotted line labeled a_{Ge}. Routine growth has been demonstrated for 7% Sn on both Si(100) and Ge(100). The growth procedure involves typical wafer pre-deposition cleaning then heating in a reactor to 350-375° C. High-purity digermane diluted in H_2 flows over the wafer for 2 min at 10^{-4} Torr to remove residual surface contaminants. Layers of defect-free and fully commensurate interfaces are grown at typical rates of 10-15 nm/min [25]. Tunable direct bandgaps ranging from 0.8-1.4 eV are possible for $Si_xGe_{1-x-y}Sn_y$ on Ge buffered Si as shown in figure 11a. Doping sources were selected for 573.15-613.15 K stability. Boron

(B) doping was conducted with B_2H_6, and routinely yielded concentrations of $5 \times 10^{19} - 2 \times 10^{20}$ cm^{-3} as shown in figure 11b. Reflection and reciprocal space map experiments indicated that mosaicities and threading dislocations are neglible [26].

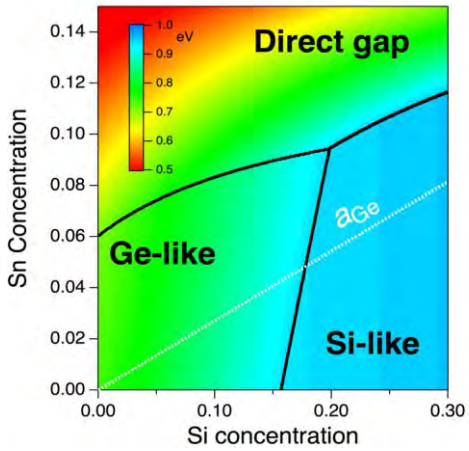

Figure 10. The dependence of the $Si_xGe_{1-x-y}Sn_y$ direct bandgap energy on Si and Sn alloy concentration is shown graphically [27]. The white dotted line represents the Sn and Si concentration required to lattice match with Ge.

SiGeSn alloys grown on Si(100) or Ge-buffered Si substrates remain stable at temperatures beyond 1073.15 K (depending on composition). Lattice matched SiGeSn to Ge revealed mobilities comparable to those in elemental Ge and produced negligible alloy scattering [9]. *p*-type doping with $p = 2 - 3 \times 10^{17}$ cm^{-3} was reduced to 5×10^{16} cm^{-3} with rapid thermal annealing and a mobility of 250 cm^2/V•s was measured [28]. The same article demonstrated the decoupling of band structure and strain.

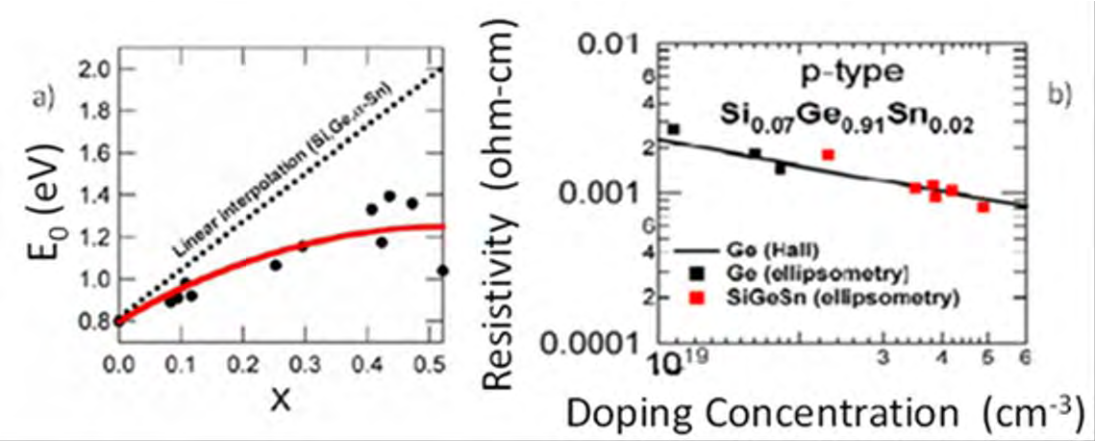

Figure 11. a) Direct bandgap E_0 as a function of (Si+Sn) fraction X, for $Ge_{1-X}(Si_{0.8}Sn_{0.2})_X$ alloys. The solid line represents the best fit of the data indicating that the gap reaches a maximum value and then decreases. b) Electrical resistivity as a function of carrier concentration of B-doped SiGeSn and corresponding reference data for bulk Ge. The black line and black squares in the figure represent published results and ellipsometry measurements, respectively [9].

The only reported PL for SiGeSn was measured at 10 K for a sample grown on GeSn having a 7% Sn concentration as shown in figure 12. The authors reported that the PL signal could be quenched by the presence of trace amounts of non-radiative recombination centers and that routine PL signal was not obtainable [29].

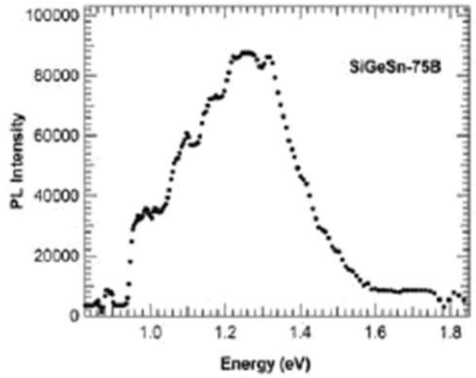

Figure 12. Band-to-band transition PL from a SiGeSn layer with 7% Sn at 10 K [29].

Sample Set and Experimental Setup

1.8 Samples

Five sample types were investigated in this study. The labels of the samples are GSSGE13b, GSSGE36b, GSSGE39b, GSSGE40b and GSSGE13cRTA, and the corresponding epilayer thicknesses, boron doping concentrations measured by SIMS, and alloy percentages are listed in table 2.

All samples are *p*-type at room temperature, B being the intentional dopant. The substrates of the four 2% Sn samples are *p*-Ge, and the 2.8% Sn sample was grown on *n*-Si substrate. The *p*-Ge substrate thickness was reported to be 280 μm thick. The *n*-Si had no reported substrate thickness value, but was estimated to be 500 μm. The samples varied in sizes and shapes, nominal sample sizes were 5 mm × 5 mm and no bigger than 2 cm × 1 cm. From figure 10, one can infer that all of these structures should be indirect gap materials, and from figure 11a, the direct bandgap should be at approximately 0.85 eV.

Table 1. Values of Epilayer Thickness, Boron Doping Concentration Measured by SIMS, and Alloy Content (from grower)

Sample	GSSGE13b	GSSGE36b	GSSGE39b	GSSGE40b	GSSGE13cRTA
Film Thickness	900 nm	800 nm	750 nm	600 nm	550 nm
Boron Concentration	Undoped	1E18 cm^{-3}	7E17 cm^{-3}	3E17 cm^{-3}	Unknown
Alloy	$Si_{0.08}GeSn_{0.02}$	$Si_{0.08}GeSn_{0.02}$	$Si_{0.08}GeSn_{0.02}$	$Si_{0.08}GeSn_{0.02}$	$Si_{0.112}GeSn_{0.028}$
Substrate	*p*-Ge	*p*-Ge	*p*-Ge	*p*-Ge	*n*-Si

Samples were grown via UHV-CVD with novel precursors. The four samples ranging from 600-900 nm film thickness had striations on the back of the polished substrate, possibly indicating spectroscopic ellipsometry measurements had been performed prior to receiving the samples. The sample with *n*-Si substrate had an unpolished back surface.

1.9 Photoluminescence

An Ar^+-laser was electrically pumped at 8 W and used to optically pump a Ti-Sapphire laser. The Ti-Sapphire laser at a wavelength of 830 nm was used to interrogate samples mounted with a thin layer of silicone to a Helitran cold finger as shown in figure 13. The laser light was modulated by a chopper at 80-83 hertz prior to transmitting through an aspheric lens which focused the beam to a spot size of approximately 150 μm. The aspheric lens allowed for an average intensity of approximately 4.3 kW/cm^2 when 0.5 W output laser power was used. The output power was measured between the Ti-Sapphire laser and the chopper. The Helitran was pumped down to 20 mTorr and cooled to approximately 7 K with evaporated helium. A purge tube was constructed and connected to the collimating lens and the SPEX 500M monochromator, both filled with nitrogen gas. The monochromator used a 600 groves-per-mm grating blazed at 1.6 μm.

A 1050 nm long-pass filter was placed at the entrance of the monochromator.

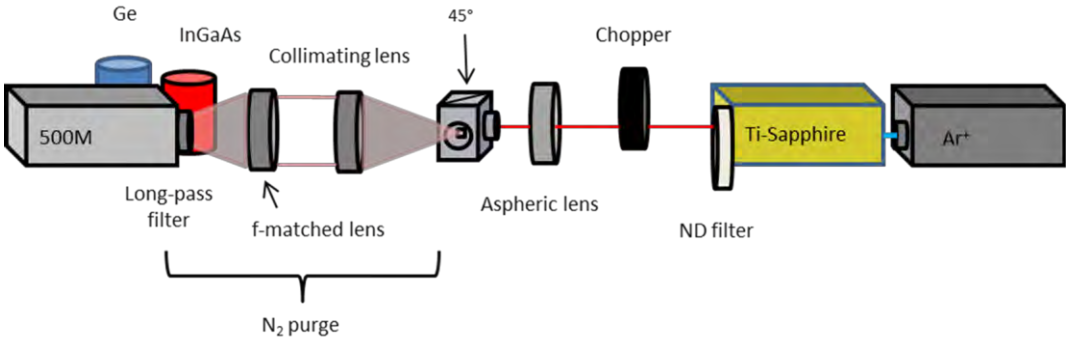

Figure 13. Photoluminescence experimental setup. A Ti-Sapphire laser, at 830 nm is focused to approximately 150 µm on the Helitran cold finger under vacuum. The luminescence at 45° is collimated and then focused down by a lens f-matched to the monochromator. The Ge detector is mounted on the side and the InGaAs is mounted on the front of the monochromator. A nitrogen purge tube was connected to both the monochromator and collimating lens.

An electrically cooled InGaAs detector with a range of 500-2300 nm and a liquid nitrogen cooled North Coast Ge detector with a range of 1000-1800 nm were mounted to the front and side of the monochromator, respectively. The Ge detector is about three orders of magnitude more sensitive at its peak responsivity when compared to InGaAs peak responsivity. (Sensitivity figures are shown in Appendix B and C.) The InGaAs detector output was fed directly into the lock-in amplifier. The Ge detector output was fed into a North Coast model 829B muon filter and the lock-in amplifier. The muon filter settings were 100 ms hold, 1 s integration time, and a gain of 50 mV. Entrance and exit slit widths, on the monochromator were 3 mm, unless specified otherwise. This results in a 10 meV resolution for this monochromator at 1.4 µm. A LakeShore 331 temperature controller was used to control the temperature of the cold finger. Two measurements of temperature were made by the temperature controller, one at the top of the cold finger and one near the bottom of the cold finger. Both sites made use of a Si diode for

temperature measurements. The temperatures cited below were measured from the bottom diode on the cold finger.

1.10 Hall Effect

Electron-beam deposition of 200 Å of Cr, followed by 2000 Å of Au on the four corners of a 5-mm square sample was used for ohmic contacts. The high and low temperature LakeShore Hall effect measurement apparatus were used. (See Appendix A.) Indium was used to connect the ohmic contacts of samples to the low temperature cold finger measurement leads. The cold finger was pumped down to less than 20 mTorr and cooled with a helium compressor. A magnetic field of 4 kG was applied.

The high temperature station used four probes that were tightened into the ohmic contacts of the samples and was also pumped down to less than 20 mTorr. A magnetic field of 3 kG was applied. I-V curves were measured prior to all temperature dependent Hall effect measurements. The two measurement systems allowed for variation in temperature from approximately 20 K to 700 K.

1.11 Transmission

Fourier transform infrared spectroscopy (FTIR) measurements were obtained using an MB157S manufactured by ABB. The sources, over the range measured, were a quartz-halogen lamp and a SiC globar. The detector is a doped triglycine sulfate detector. The range of the FTIR was 7800-450 cm^{-1}. A number of resolution settings are available on the FTIR. The 4 cm^{-1} resolution was the setting of choice for the following experiments, and 400 scans were averaged. Considering that the signal to noise ratio is $1/\sqrt{scans}$ this was enough to reduce the noise level considerably. Spectra taken using a

128 cm^{-1} resolution and an average of 4000 scans were also made for comparison. The lower resolution gives much higher signal to noise ratio and allows for identification of broader features. An absorbance of up to 6 OD is possible with the lowest resolution. No novel features were observed with the lower resolution settings.

A background scan was performed prior to all transmission measurements, and both background and transmission measurements had the same resolution and number of scans. A mounting stage with a 0.5 cm diameter port was used. A thin layer of silicone on the edge of the mounting portal was employed because the typical mounting brackets were too large to hold the samples.

The FTIR uses a Michelson-type interferometer. The optical path difference is measured and an interferogram is created. A Fourier transform algorithm is then employed to return the results in a transmission plot.

Experimental Data and Analysis

1.12 Photoluminescence

Systematic position-dependent measurements were made for each sample. No room temperature luminescence of the SiGeSn epilayer was observed. The strong luminescence of the *p*-type Ge substrate was observed at room temperature. Each sample was cooled to 7 K and luminescence was measured with both InGaAs and Ge detectors. PL of the sample with 600 nm thick epilayer exhibited weak luminescence of the epilayer at 2 orders of magnitude less than the substrate. This weak PL persisted up to 75 K. The *p*-Ge transverse acoustical (TA) phonon assisted and no-phonon indirect bandgap PL could be observed with the InGaAs detector at 0.71 eV and 0.738 eV, respectively. This was true for all *p*-$Si_{0.08}Ge_{0.90}Sn_{0.02}$ /*p*-Ge measured. The *p*-$Si_{0.08}Ge_{0.90}Sn_{0.02}$ peak could not be observed while using the InGaAs detector as shown in figure 14. Switching to the more sensitive Ge Detector, the *p*-$Si_{0.08}Ge_{0.90}Sn_{0.02}$ epilayer PL may have been identified with 3mm slits and 200 microvolt sensitivity as shown in figure 15. The resolution of this monochromator at 1.4 μm was estimated to be 10 meV. The signal is hampered with noise and any indication of indirect or direct bandgap could not be resolved.

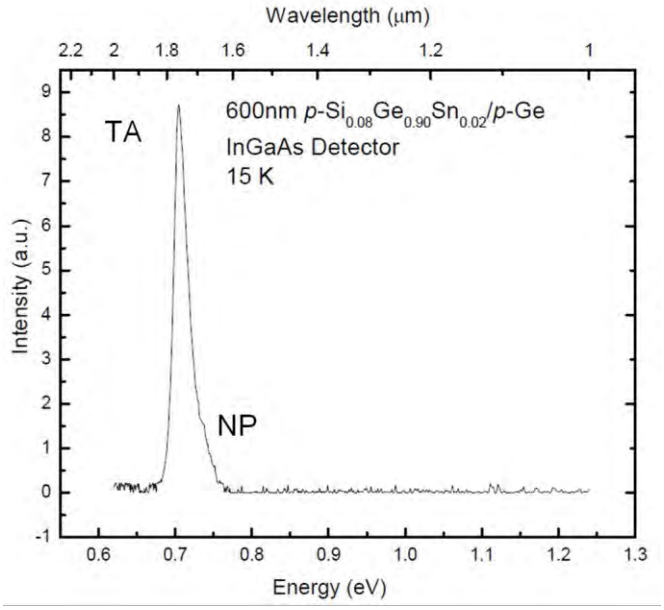

Figure 14. Photoluminescence as a function of energy for the 600 nm thin film, measured at 15 K with the InGaAs detector. The TA phonon and no phonon PL of the indirect gap of the Ge substrate can be observed using the InGaAs detector.

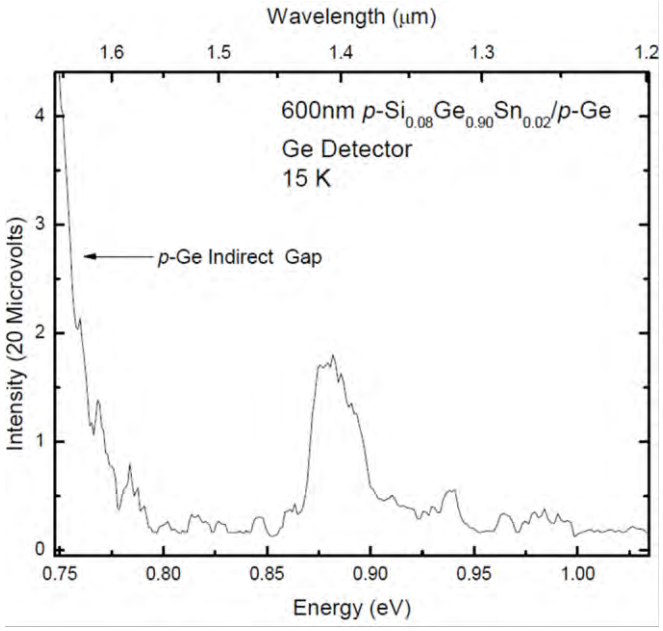

Figure 15. Photoluminescence as a function of energy for the 600 nm thin film, measured at 15 K with the Ge detector. The onset of the luminescence, for the peak shown, is 0.868 eV.

1.13 Transmission Measurements

In this section, interference fringes were used to calculate the thickness of *p*-Ge substrate. A value of 133 ± 6 μm was measured, which is different from the growers reported 280 μm thickness. A micrometer was then used to measure the thickness of two of the *p*-$Si_{0.08}Ge_{0.90}Sn_{0.02}$ /*p*-Ge samples and a value of 140 μm was measured. Transmission measurements showed valence band absorption peaks at 0.29 eV and 0.37 eV attributed to the epilayer of *p*-$Si_{0.08}Ge_{0.90}Sn_{0.02}$. An effective mass calculation was performed and values of $m_{hh} = 0.30m, m_{lh} = 0.051m, m_{so} = 0.79m$ and $\Delta\epsilon = 0.30\ eV$ were obtained. The unexpected peak at 0.37 eV is possibly due to the non-parabolicities of the SiGeSn hh and lh bands. The *p*-$Si_{0.112}Ge_{0.86}Sn_{0.028}$/*n*-Si sample was measured to have an indirect bandgap absorption edge at 0.780 eV and a direct bandgap edge at 0.845 eV. In the following absorption measurements, to be completely accurate, one has to take into account reflectivity. Reflectivity measurements were performed, however, the small sample sizes introduced large uncertainty in measurement, and thus results were not included. The use of transmission was employed solely, although some error was introduced.

Transmission measurements made with the FTIR introduce interference fringes associated with the substrate thickness as shown in figure 16. A simple calculation to verify substrate thickness was performed using $4\pi nd\left(\frac{1}{\lambda_1} - \frac{1}{\lambda_2}\right) = 2\pi$, with a value of *n* = 4 for Ge. The calculated value of thickness, *d,* for the 4 samples was 133 μm with an 86% accuracy within 6 μm, a much-different-than-reported value of 280 μm by almost a factor of 2. A micrometer was then used to measure the thickness to verify these results.

Measurements of the samples with 750 and 600 nm epilayer thickness yielded values of 140 μm. For reference a 500 μm thick Ge wafer was measured with the same micrometer yielding a value of 505 μm.

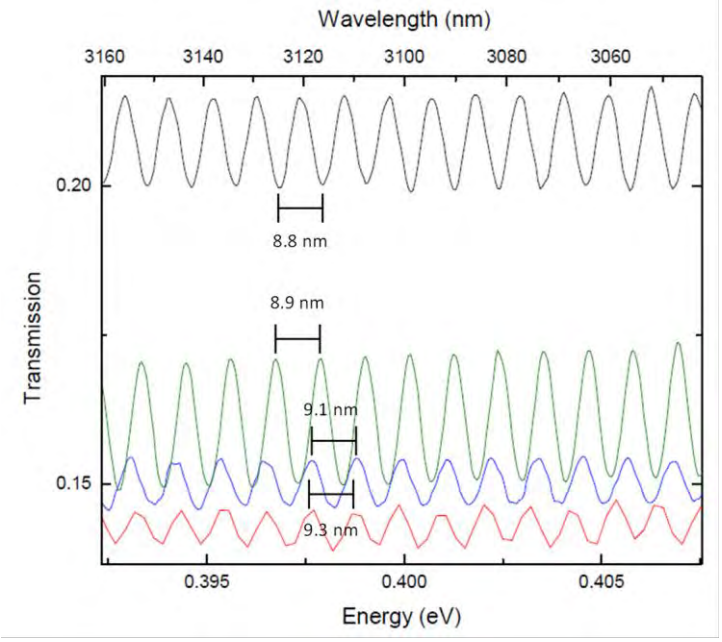

Figure 16. Transmission as a function of energy. Interference fringes from the substrate can be identified. Using the difference in wavelength for each fringe a calculation of the substrate thickness resulted in 133 ± 6 μm. From top to bottom, 900, 600, 750 and 800 nm thick epilayer samples.

Considering that the *p*-$Si_{0.08}Ge_{0.90}Sn_{0.02}$ samples were grown on *p*-type Ge, and the expected direct band edge of the epilayer material is approximately 0.85 eV, as shown in figure 11a, conduction band to valence band absorption of the thin film cannot be interrogated with transmission measurements because the Ge direct gap absorption occurs at lower energy. However, intervalence band absorption can be examined as shown in figure 17. The band to band transition of the *p*-$Si_{0.112}Ge_{0.86}Sn_{0.028}$/*n*-Si was measured and

is discussed below. The use of absorbance, instead of absorption coefficient, was employed due to the combining of absorption of both epilayer and substrate.

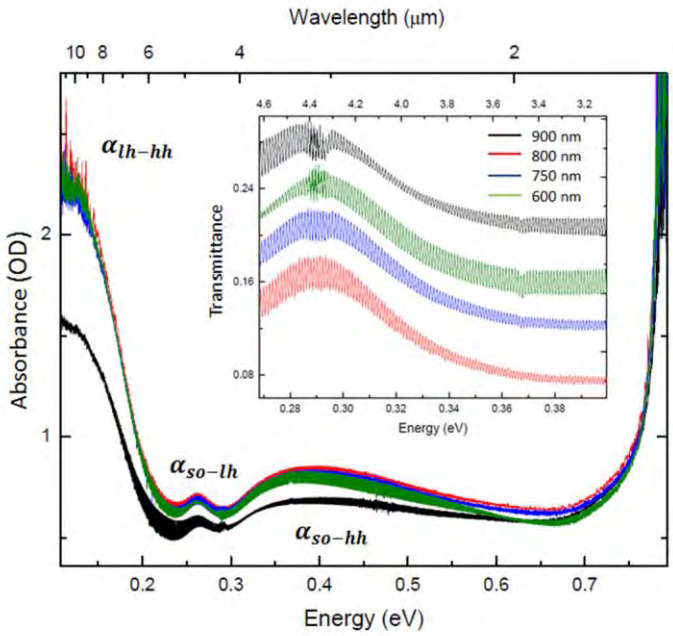

Figure 17. Absorbance as a function of energy for the *p*-$Si_{0.08}Ge_{0.90}Sn_{0.02}$ /*p*-Ge samples. lh-hh, so-lh, and so-hh transitions can be identified. Inset: Raw transmittance measurements, displaced for clarity, in the region of so-lh interband transition. From top to bottom: the 900, 600, 750, 800 nm epilayer thick thin film samples.

1.13.1 Transmission Measurements of *p*-$Si_{0.08}Ge_{0.90}Sn_{0.02}$/*p*-Ge

The absorbance as a function of energy is shown in figure 18. Absorption relating to lh-hh, so-lh, and so-hh bands is identified for the four *p*-$Si_{0.08}Ge_{0.90}Sn_{0.02}$ /*p*-Ge samples in figure 18. Using equations (2.14) and (2.15), a theoretical model for the absorption coefficient for each valence band transition was developed and is shown at the bottom of figure 18. The use of a Gaussian line shape was employed for the lh→so transition. The fit parameters are enumerated in table 2 along with effective mass parameters for other group IV materials. In table 2, the Ge and Si data are taken from [20] and the α-Sn data

is taken from [30]. The model does not fit exactly for several reasons. First, the assumptions and simplifications made in the derivation of equations 2.13-2.15, such as parabolic bands and a Boltzmann distribution of charge carriers introduce some fitting error. Second, the imperfections in the sample, such as the striations on the back surface, most certainly caused some artificial increase in absorption in the measurement. Finally, considering the doping levels of the samples, free carrier absorption in this regime could account for additional deviation from the fitted model, α_{Total}.

Table 2. Interband Absorption Fit Parameters of *p*-$Si_{0.08}Ge_{0.90}Sn_{0.02}$/*p*-Ge Compared with other Group IV Elements

Name	m^*_{hh}	m^*_{lh}	m^*_{so}	$\Delta\epsilon$
p-$Si_{0.08}Ge_{0.90}Sn_{0.02}$/*p*-Ge	$0.30m_e$	$0.051m_e$	$0.79m_e$	$0.30\ eV$
Ge	$0.3m_e$	$0.04m_e$	$0.095m_e$	$0.275^{\dagger}\ eV$
Si	$0.54m_e$	$0.15m_e$	$0.23m_e$	$0.044\ eV$
α-Sn	$0.195m_e$	$0.058m_e$	$0.04m_e$	$(0.413^{\dagger\dagger})0.8\ eV$
Unknown	$0.3m_e$	$0.075m_e$	$0.79m_e$	0.37 eV

1† Differing from initial value of 0.3eV from [20]
1†† Energy difference between hh and lh bands. [30]

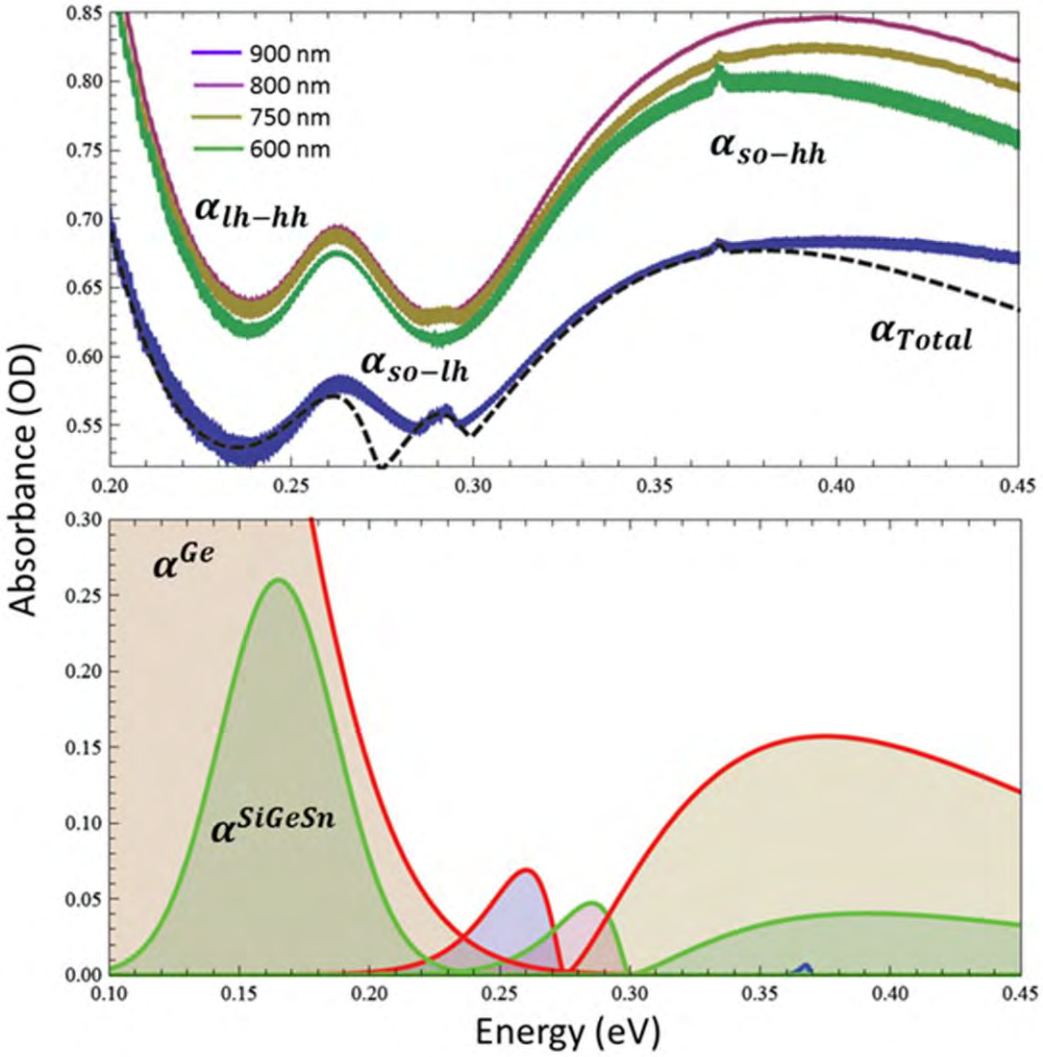

Figure 18. Top) The absorbance as a function of energy for the samples with 900, 800, 750, and 600 nm thick epilayers, measured at room temperature. The dashed black line, α_{Total}, is the combined absorption for the intervalence band transitions of the substrate and epilayer. Bottom) The individual absorptions for the different intervalence band transitions, the Urbach tail of Ge is not depicted. The red line shapes correspond to the absorption of the *p*-Ge substrate. The green line shapes correspond to the *p*-$Si_{0.08}Ge_{0.90}Sn_{0.02}$ epilayer. The blue line shape corresponds to an unidentified absorption.

There has been a local density approximation (LDA) theoretical study done using a 64-atom diamond lattice supercell of $Si_{0.44}Ge_{0.45}Sn_{0.11}$ which shows a splitting in hh and lh bands. However, these alloy concentrations are much different than the sample sets characterized here [27], thus the estimated effective masses could not realistically be

compared to those reported in the LDA study. For the unknown transition, considering the hh and so masses are the same as those in SiGeSn, the values lh and $\Delta\epsilon$ could be due to some residual strain that has been reported to shift the lh band above the hh band [31]. To date, there has not been any exhaustive theoretical studies on the band structure of SiGeSn, as there have been for Ge-Sn and strained Ge on SiGeSn. These measured data should prove to be useful in validating future studies on band structure and the effective mass of SiGeSn.

1.13.2 Transmission Measurements of *p*-$Si_{0.112}Ge_{0.86}Sn_{0.028}$/*n*-Si

Considering that the onset of the indirect and direct bandgap absorption of *p*-$Si_{0.112}Ge_{0.86}Sn_{0.028}$/*n*-Si epilayer occurs at lower energy than the Si substrate, approximately 1.12 eV, measurement of *p*-$Si_{0.112}Ge_{0.86}Sn_{0.028}$ band to band transitions could be made. The indirect bandgap absorption is shown in figure 19. A best fit corresponded to the indirect bandgap energy of 0.780 eV. Significant scattering, resulting from the unpolished back surface of the sample, is observed as an increase in absorbance of about 1 OD. Free carrier absorption was also observed in the measured data, as shown prior to the onset of the indirect bandgap of *p*-$Si_{0.112}Ge_{0.86}Sn_{0.028}$ in figure 19.

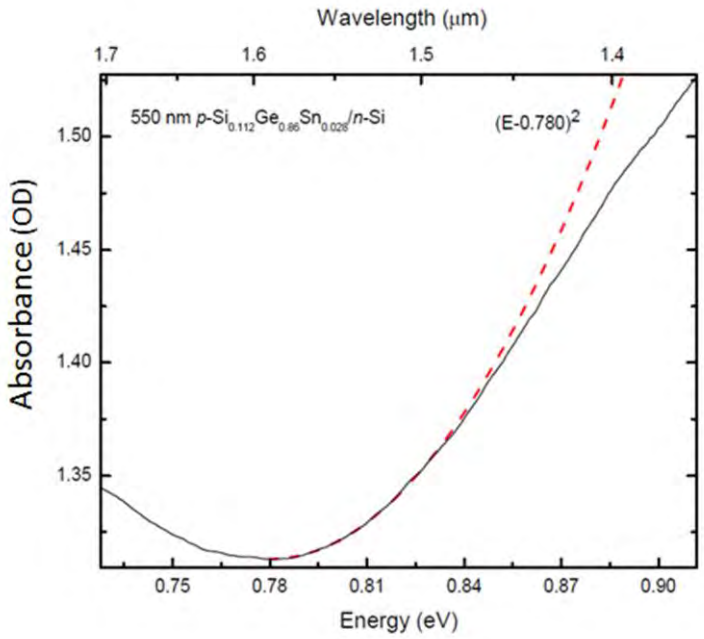

Figure 19. Absorbance of p-$Si_{0.112}Ge_{0.86}Sn_{0.028}$/$n$-Si as a function of energy measured at room temperature. The indirect gap of the epilayer is estimated to be at 0.780 eV. Free carrier absorption is observed below the onset of the indirect bandgap. Scattering from the back of the sample surface is the cause of the increased absorbance prior to the onset of the interband absorption.

To obtain an estimate of the absorption coefficient of p-$Si_{0.112}Ge_{0.86}Sn_{0.028}$, the absorption was normalized to the onset of the indirect bandgap absorbance and a semi-log plot of the absorption coefficient was generated as shown in figure 20. The direct bandgap of p-$Si_{0.112}Ge_{0.86}Sn_{0.028}$ was estimated to be at 0.845 eV. This is close to predicted values of 0.85 eV and also corresponds to a critical point observed in ellipsometric measurements. (See Appendix E.) The value of the absorption coefficient above the direct bandgap of p-$Si_{0.112}Ge_{0.86}Sn_{0.028}$ is similar to that of Ge above the direct band edge reported by [32].

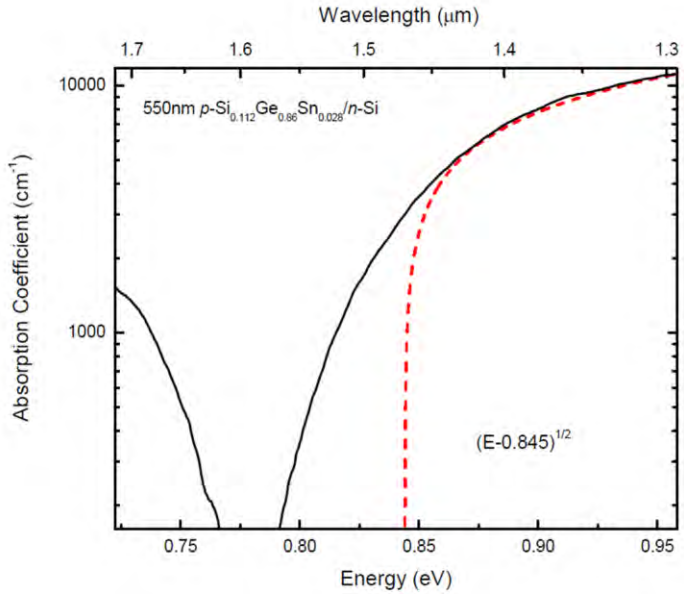

Figure 20. The absorption coefficient of p-$Si_{0.112}Ge_{0.86}Sn_{0.028}$/$n$-Si measured at room temperature. The direct bandgap of the epilayer is estimated to be at 0.845 eV.

1.14 Hall Effect Measurements

The sheet carrier concentrations at room temperatures of all four p-$Si_{0.08}Ge_{0.90}Sn_{0.02}$/$p$-Ge samples were estimated to be $4.35 \times 10^{15}, 8.80 \times 10^{15}, 1.33 \times 10^{16}$, and $8.21 \times 10^{15}\ cm^{-2}$ for the samples with 900, 800, 750, and 600 nm epilayer thickness, respectively. The higher carrier concentrations observed for these samples are affected by the hole mobilities which were estimated to be 672, 468, 367, and 547$cm^2/V\bullet s$ for the samples with 900, 800, 750, and 600 nm epilayer thickness, respectively. The undoped p-$Si_{0.08}Ge_{0.90}Sn_{0.02}$/$p$-Ge changed conductivity type at 675 K. At low temperatures, the carrier mobility was mainly affected by ionized impurity scattering, but at high temperature it was mainly affected by lattice scattering and alloy scattering. The uncorrected acceptor activation energy was estimated to be 3 meV for the four p-$Si_{0.08}Ge_{0.90}Sn_{0.02}$/$p$-Ge samples. Considering that the acceptor level for boron

doped GeSn and boron doped $Si_{0.112}Ge_{0.86}Sn_{0.028}$/*n*-Si are estimated to be 10 meV [33] and a rise in carrier concentration was observed at low temperatures, a multilayer model was employed to determine the corrected acceptor level of 10.7 meV. The resistivities of the four *p*-$Si_{0.08}Ge_{0.90}Sn_{0.02}$/*p*-Ge samples were estimated to be $1.82 \times 10^{-4}, 1.12 \times 10^{-4}, 0.93 \times 10^{-4}$, and 0.84×10^{-4} ohm-cm at room temperature for the samples with 900, 800, 750, and 600 nm epilayer thicknesses, respectively.

The Hall effect measurements of the *p*-$Si_{0.112}Ge_{0.86}Sn_{0.028}$/*n*-Si sample were conducted during a previous effort by Dr. M. Ryu at the Air Force Institute of Technology, and are discussed in Appendix F.

1.14.1 Carrier Concentration

The results of Hall effect measurements of the four *p*-$Si_{0.08}Ge_{0.90}Sn_{0.02}$ /*p*-Ge samples are plotted in figure 21. The sheet carrier concentration (SCC), cm^{-2}, was used instead of the carrier concentration, cm^{-3}, due to participation of an interfacial layer and *p*-Ge substrate. The SCC decreases slightly with increasing temperature from 30 to 100 K for the 800 and 750 nm thick films. The 900 and 600 nm thick films' SCC decreases as the temperature increases from 30 to 90 K. This slight decrease in carrier concentration is due to multiple conducting layers of the substrate, the interfacial, and the epitaxial layer. The carrier concentration is constant from ~100 K to ~450 K as shown in figure 21. The carrier concentration in this regime, which is largely independent of temperature, is due to the boron dopant concentration in each sample as well as the participation of the interfacial layer and substrate. Just below around 450 K, there is a small peak in carrier concentration. This has been reported for samples of GeSn. A similar transport process must occur in these samples, although the type conversion does

not occur in all of samples in the regime reported due to high acceptor concentrations. Above 600 K, the typical exponential increase in the concentraion of intrinsic carriers is observed.

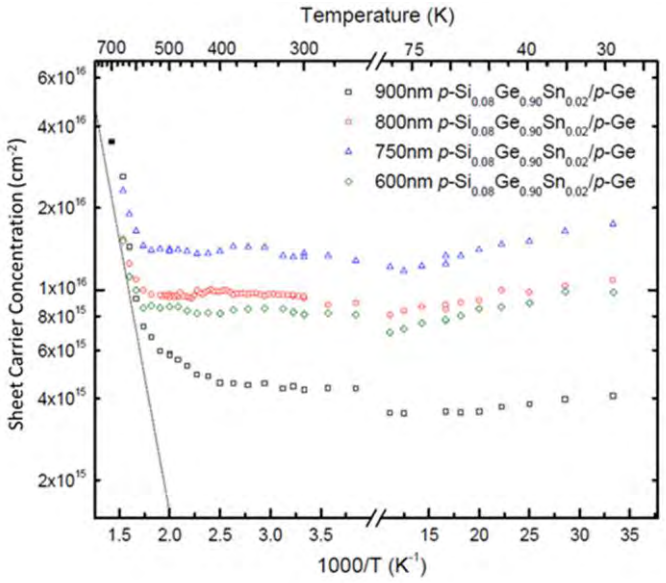

Figure 21. Semi-log plot of sheet carrier concentration as a function of inverse temperature. The samples with epilayer thicknesses of 900, 800, 750, and 600 nm are depicted as square, circle, triangle, and diamond respectively. A type conversion to *n*-type occurs for the 900 nm sample at 675 K. The line indicates the intrinsic carrier concentration for *p*-type Ge with a direct bandgap energy value of 0.80 eV. The rise in carrier concentration in the low temperature regime indicates multiple conducting layers in the sample.

1.14.2 Mobility

The peak mobilities for the *p*-$Si_{0.08}Ge_{0.90}Sn_{0.02}$/*p*-Ge layers are 1210, 836, 752, and 568 $cm^2/V•s$ for the 900, 600, 800, and 750 nm thick samples, respectively, as shown in figure 22. The mobility is highest for the lowest doped sample (900 nm thick sample), and the mobility decreases as the doping level increase. The mobilities at room temperature are about half of that reported for thin films of *p*-Ge, 700-800 $cm^2/V·s$ [34].

The peak in mobility with respect to temperature shifts to higher temperature with increasing doping concentration; this has also been observed in increasing concentrations

of Sn content for GeSn samples. A decrease in mobility with increasing Sn concentration, due to increased alloy scattering, has been observed in similar samples [33].

In the low temperature regime, the mobility, μ, is mainly proportional to temperature by $\mu \sim T^{\frac{3}{2}}$. This is primarily affected by ionized impurity scattering, which has been shown to have a temperature dependence of $\mu \sim T^{\frac{3}{2}}$ [11]. In the high temperature regime the mobility is mainly affected by both alloy and lattice scattering. It is well known that mobility due to lattice scattering in Ge has a temperature dependence of $T^{-2.3}$ [23] and the termperature dependence of alloy scattering in GeSn has been shown to be proportional to $\mu \sim T^{-\frac{1}{2}}$ [33]. Using Matthiessen's rule, a best fit for the mobility μ was obtained and is shown in figure 22.

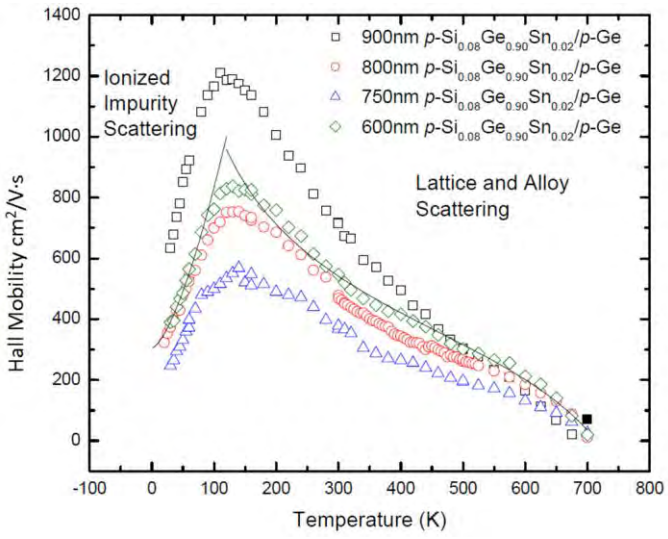

Figure 22. The Hall mobility as a function of temperature for the four *p*-$Si_{0.08}Ge_{0.90}Sn_{0.02}$ /*p*-Ge samples measured. The samples with epilayer thicknesses of 900, 800, 750, and 600 nm are depicted as square, circle, triangle, and diamond, respectively. *n*-type carriers are filled in shapes. A best fit for ionized impurity, lattice, and alloy scattering is shown as the black line.

1.14.3 Conductivity

Temperature dependent conductivities are plotted in figure 23 for the *p*-$Si_{0.08}Ge_{0.90}Sn_{0.02}$/*p*-Ge samples. From these data, the activation energy of the acceptor can be obtained from the equation

$$\sigma = (N_v N_a)^{1/2} e^{\frac{-(E_v - E_a)}{kT}}, \quad (0.1)$$

where N_v is the concentration of holes in the valence band, N_a is the concentration of acceptor dopants, k is Boltzmann's constant, T is the temperature, and $(E_v - E_a)$ is the acceptor activation energy. The best fits for the acceptor activation energy are around 3.0 meV for all samples. Because these samples were intentionally doped with B, we can compare this value to the acceptor activation energy with those reported in the literature. The acceptor activation energy for boron doped Si is 40 meV and for boron doped Ge is 10 meV. The acceptor activation energy for boron doped *p*-$Si_{0.112}Ge_{0.86}Sn_{0.028}$/*n*-Si has been estimated to be 10 meV while that of boron doped GeSn is 10 meV [33]. The lower estimate of 3 meV for the four *p*-$Si_{0.08}Ge_{0.90}Sn_{0.02}$ /*p*-Ge samples stems from multiple conducting layers. Further evidence of this can be observed in the participation of these layers in Hall effect measurements by the unexpected appearance of a deeper donor at temperatures below 50 K.

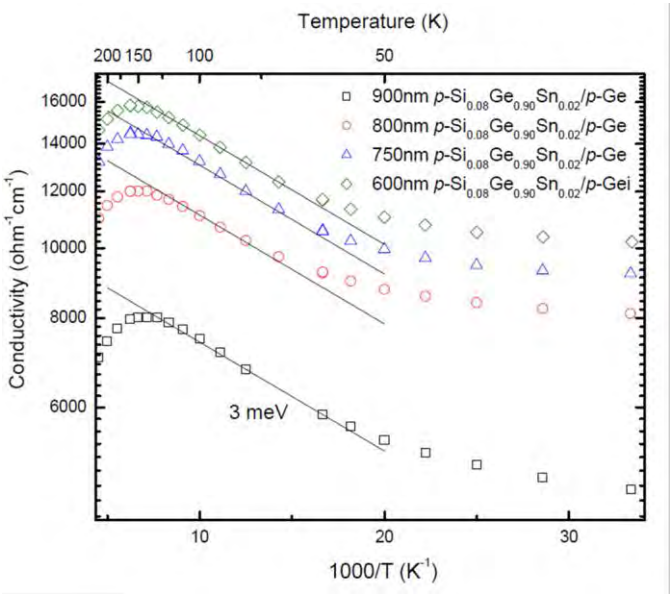

Figure 23. The conductivity as a function of inverse temperature, based upon Hall effect measurements. Multiple conducting layers falsely reduce the activation energy and a deeper donor appears below 50 K. An uncorrected activation energy of 3 meV is estimated and plotted in black lines for each sample.

Using the expected value of the acceptor activation energy, 10 meV, equation (4.1), and the B-doping concentration measured by SIMS, a theoretical model of the carrier concentration in cm^{-3}, was developed. This model is depicted in figure 24, and gives an estimate of what the measured epilayer carrier concentration values would be if there were no effects from the interfacial layer and substrate.

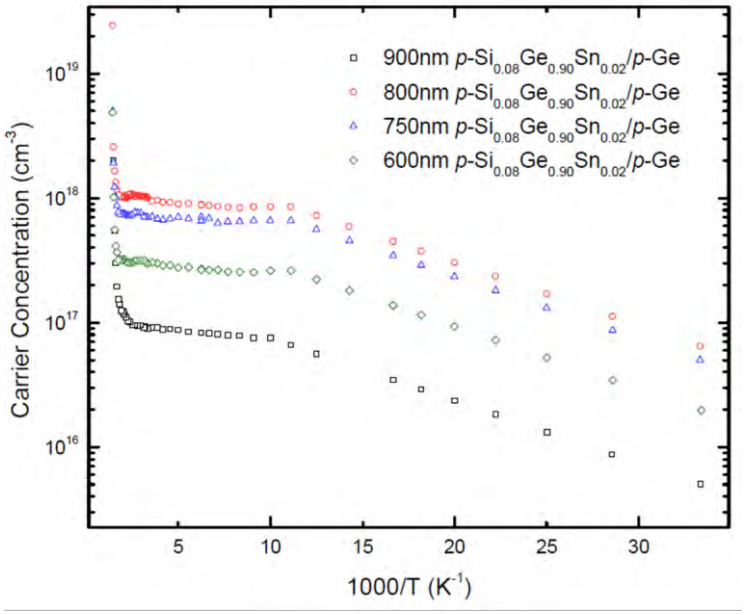

Figure 24. Semi-log plot of the theoretical carrier concentration as a function of inverse temperature for the *p*-$Si_{0.08}Ge_{0.90}Sn_{0.02}$ /*p*-Ge samples ignoring effects from the interfacial and substrate layers. The samples with epilayer thicknesses of 900, 800, 750, and 600 nm are depicted as square, circle, triangle, and diamond respectively.

1.14.4 Correcting for Multiple Conducting Layers in *p*-$Si_{0.08}Ge_{0.90}Sn_{0.02}$/*p*-Ge

The corrected acceptor level can be obtained following the derivation of equations (2.22-2.25). As discussed in section (2.6.4,) $n_{s,2}$ and μ_2, the interfacial layer's sheet carrier concentration and mobility respectively, can be obtained from the low temperature limits of the sheet carrier concentration and mobility measurements. From equation (2.24) and (2.25), the conductivity of the epilayer can be extracted by multiplying (2.24) and (2.25) together. The resulting equation then simplifies to

$$n_{s,1}\mu_{s,1} = n_s\mu_s - \frac{n_{s,2}\mu_2}{d}, \qquad (0.2)$$

where $n_{s,1}$ and $\mu_{s,1}$ are related to the corrected conductivity of the epilayer. For the four *p*-$Si_{0.08}Ge_{0.90}Sn_{0.02}$ /*p*-Ge the interfacial region carrier concentration, $n_{s,2}$, was estimated

to be $1.74 \times 10^{16}, 1.08 \times 10^{16}, 9.81 \times 10^{15}$, and $4.08 \times 10^{15}\ cm^{-2}$ for the 750, 800, 600, and 900 nm epilayer thick samples, respectively. The mobility of the interfacial layer, μ_2, was estimated to be 620, 360, 322, and 235 $cm^2/V \cdot s$ for the .900, 600, 800, and 750 nm epilayer thick samples, respectively. The measured temperature dependent data for carrier concentration and mobility, were used for n_s and μ_s, respectively and d was the thickness of the epilayer. The best fit for the four samples was 10.7 meV as shown in figure 25.

In figure 25, the deeper donor is still observed; this indicates that the method used is not exact. The difference between the 10.7 meV fit and of the acceptor level and the expected 10 meV acceptor level arise for two reasons. The first is that the interfacial region conductivity is approximated by a constant mobility and carrier concentration. Considering that neither the carrier concentration nor mobility of the interfacial layer changes with temperature in this model, there is no way to remove the appearance of the deeper donor. Additionally, only the two layer model was used in this case. In order to obtain a more accurate estimation of the acceptor level, the three layer model must be used and thus a measurement of the back of each sample must be made, although the mathematics will be similar as described in section (2.4.4).

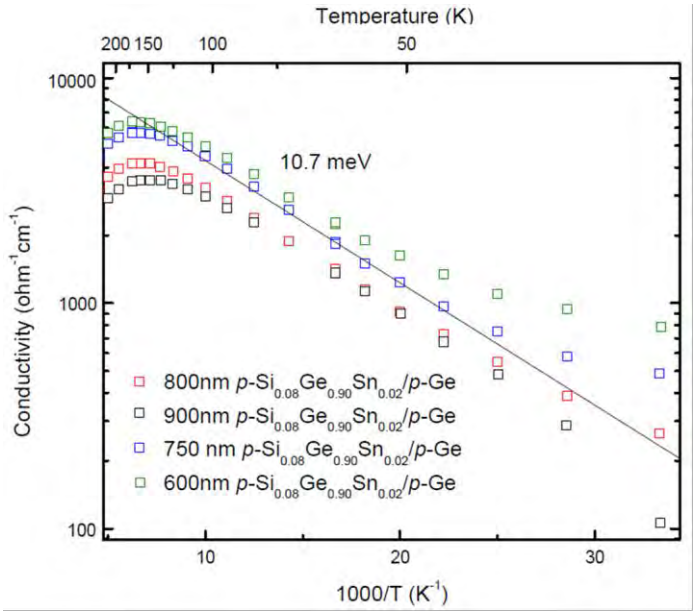

Figure 25. The conductivity as a function of inverse temperature, based upon corrected Hall effect measurements. A corrected activation energy of 10.7 meV is estimated and plotted as the black line. A deeper donor still appears below 50 K. This is due to the temperature indepent approximation of sheet carrier concentration and mobility for the interfacial layer model.

1.14.5 Carrier Concentration Measurements on the *p*-Ge Substrate

Hall effect measurements were also done on the back of each of the four *p*-$Si_{0.08}Ge_{0.90}Sn_{0.02}$/*p*-Ge samples to determine the effect of the *p*-doped substrate as shown in figure 26. These measurements show the effect of *p*-Ge substrate is very high on the estimation of *p*-$Si_{0.08}Ge_{0.90}Sn_{0.02}$ layer. This stems from the fact that an interfacial layer exists between the substrate and epilayer.

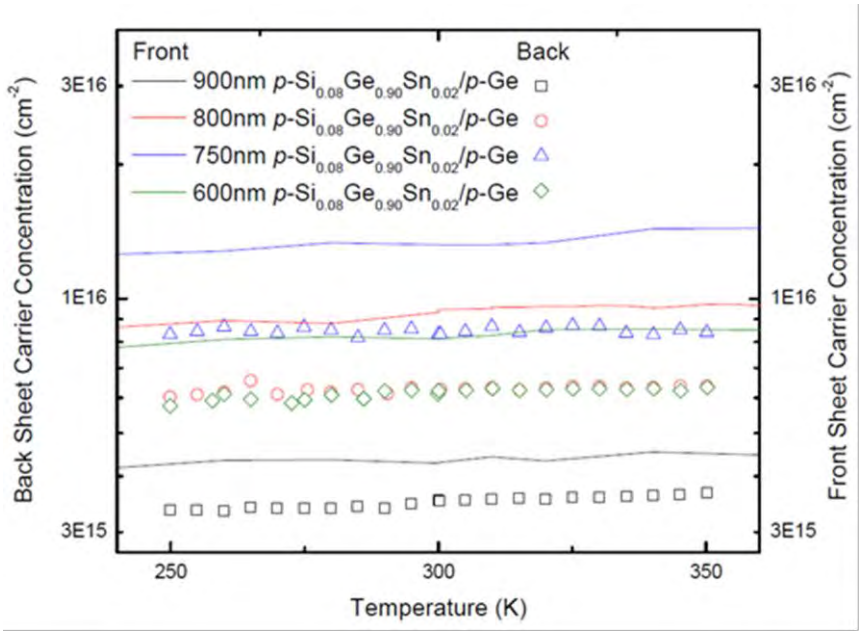

Figure 26. Sheet carrier concentration measured on the back of the *p*-$Si_{0.08}Ge_{0.90}Sn_{0.02}$/*p*-Ge samples represented as square, circle, triangle and diamond for the samples with epilayer thicknesses of 900, 800,750, and 600 nm, respectively. Front of sample sheet carrier concentration are represented as lines in the same order. Similar trends in the measurements of the front and back of the samples indicate and interfacial layer has formed at the substrate and epilayer interface.

Summary and Recommendations

1.15 Summary of Research

The results of room temperature Hall effect measurements are shown in table 3. The 900 nm thick epilayer *p*-$Si_{0.08}Ge_{0.90}Sn_{0.02}$/*p*-Ge showed a conductivity type change at 675 K. In the low temperature regime, the mobility is mainly affected by ionized impurity scattering. In the high temperature regime, the mobility is mainly affected by lattice and alloy scattering.

Table 3. Room Temperature Hall Effect Data

Sample ID	Sample with alloy concentration	Substrate	Epilayer/ substrate thickness [nm/μm]	Resistivity [Ohm-cm]	Sheet carrier concentration [cm^{-2}]	Hall mobility [$cm^2/V•s$]	Acceptor activation energy [meV]
13b	*p*-$Si_{0.08}Ge_{0.90}Sn_{0.02}$	*p*-Ge(100)	900/133±6	1.82E-04	4.28E+15	717.3661	10.7
36b	*p*-$Si_{0.08}Ge_{0.90}Sn_{0.02}$	*p*-Ge(100)	800/133±6	1.12E-04	9.32E+15	478.44327	10.7
39b	*p*-$Si_{0.08}Ge_{0.90}Sn_{0.02}$	*p*-Ge(100)	750/133±6	9.33E-05	1.32E+16	378.67018	10.7
40b	*p*-$Si_{0.08}Ge_{0.90}Sn_{0.02}$	*p*-Ge(100)	600/133±6	8.42E-05	8.13E+15	547.26893	10.7
13c	*p*-$Si_{0.112}Ge_{0.86}Sn_{0.028}$	*n*-Si(100)	550/500	0.17127	1.21E+13	166.49	10

Transmission measurements showed intervalence band absorption peaks at 0.29 eV and 0.37 eV from the epilayer of *p*-$Si_{0.08}Ge_{0.90}Sn_{0.02}$ /*p*-Ge. The peak at 0.37 eV is possibly due to the non-parabolicities of the hh and lh bands of the *p*-$Si_{0.08}Ge_{0.90}Sn_{0.02}$. The peak at 0.29 eV is due to the so-lh transition in *p*-$Si_{0.08}Ge_{0.90}Sn_{0.02}$. An effective mass calculation was performed, and the results are listed in table 2. The estimated

values were $m_{hh} = 0.30m, m_{lh} = 0.051m, m_{so} = 0.79m$, and $\Delta\epsilon = 0.30\ eV$. The indirect bandgap of the epilayer of *p*-$Si_{0.112}Ge_{0.86}Sn_{0.028}$/*n*-Si sample was estimated to be 0.780 eV and the direct bandgap energy value was estimated to be 0.845 eV, which is close to predicted values of 0.85 eV.

No room temperature PL of the *p*-SiGeSn epilayers was observed. The strong room temperature luminescence of the *p*-type Ge substrate direct and indirect bandgap was observed at 0.78 eV and 0.68 eV, respectively. At 15 K the substrate's no-phonon indirect luminescence was estimated to occur at 0.74 eV and the transverse acoustical phonon-assisted luminescence was 32 meV lower. At 15 K, the sample with 600 nm epilayer thickness showed luminescence of the epilayer at 2 orders of magnitude less than the *p*-Ge substrate. The onset of luminescence was at 0.885 eV.

1.16 Significance of Research

This study represents the first temperature-dependent Hall effect measurements performed on *p*-$Si_{0.08}Ge_{0.90}Sn_{0.02}$/*p*-Ge(100). The identification of an interfacial conducting layer at the interface between the substrate and epilayer was analyzed and the corrected acceptor activation energy for boron were estimated to be 10.7 meV with the two conducting layers model.

This study also conducted the first valence band transmission measurements of *p*-$Si_{0.08}Ge_{0.90}Sn_{0.02}$/*p*-Ge(100) and calculations of the hh, lh, and so band effective mass values were made. The obtained effective mass values should prove to be useful in the future theoretical and experimental analysis on SiGeSn band structure. Further, transmission measurements performed on *p*-$Si_{0.112}Ge_{0.86}Sn_{0.028}$/*n*-Si allowed for the

estimation of the direct bandgap and indirect bandgap energy values of 0.845 eV and 0.780 eV, respectively. The estimated direct bandgap energy value was 50 meV less than predicted values for this sample. The estimated indirect bandgap energy was the first reported value for the indirect bandgap for boron doped $Si_{0.112}Ge_{0.86}Sn_{0.028}$.

1.17 Recommendations for Future Research

Future research should include derivation of the alloying scattering coefficient for *p*-SiGeSn [24]. This would prove to be useful in comparing theoretical mobility dependence on temperature to experimental data. Measurements of the back side of each sample would prove to be helpful in evaluating the electrical properties of the epilayer alone. Further theoretical work should also be done to model and analyze the band structure of *p*-SiGeSn. There is currently only one theoretical band structure study that has been done but only for a single alloy concentration [27]. Reflectivity and spectroscopic ellipsometry using whole or half wafers of *p*-SiGeSn could prove to be invaluable in finding the exact energy values of the indirect and direct bandgap of future samples.

A temperature dependent study of intervalence band transitions using double sided polished whole wafers would provide for more accurate analysis of the effective masses of three valence bands. Having a double sided wafer will reduce scattering and increase the measured signal to noise ratio. As shown in [17], when reducing the temperature, the peaks from the transitions between the lh-hh bands, so-lh bands, and so-hh bands reduce and become more narrow. This is beneficial because the fit of equations (2.13)-(2.15) will be more accurate due to a decrease in overlap from the three band

transitions, assuming there is enough signal to observe the transition peaks. For *p*-Ge the lh-hh transition and so-hh transition peaks are observable at temperatures as low as 5 K [17], although the so-lh transition is unobservable at 77 K.

The low growth temperatures of 250-350 °C, bandgap engineering, and integration on various semiconductors make SiGeSn alloys an exciting and interesting topic of future research. Overall, characterization of both the direct and indirect bandgap energies as functions of Si and Sn concentration should have priority in any study of SiGeSn. Considering that the absorption coefficient of *p*-$Si_{0.112}Ge_{0.86}Sn_{0.028}$/*n*-Si was found to be comparable to Ge, SiGeSn does appear to have promising uses as a photo-detector or solar cell. This is especially true if it possible to engineer the bandgap to be 1 eV, which is currently an energy range of interest in the photovoltaic industry [25]. Use of SiGeSn as a gain medium may be possible in the future. However, more characterization of direct bandgap SiGeSn alloys is needed. Even so, SiGeSn could still be incorporated into a lasing device as a buffer layer for integration onto different semiconductor structures.

Appendix A

Hall Effect Measurement System Diagram

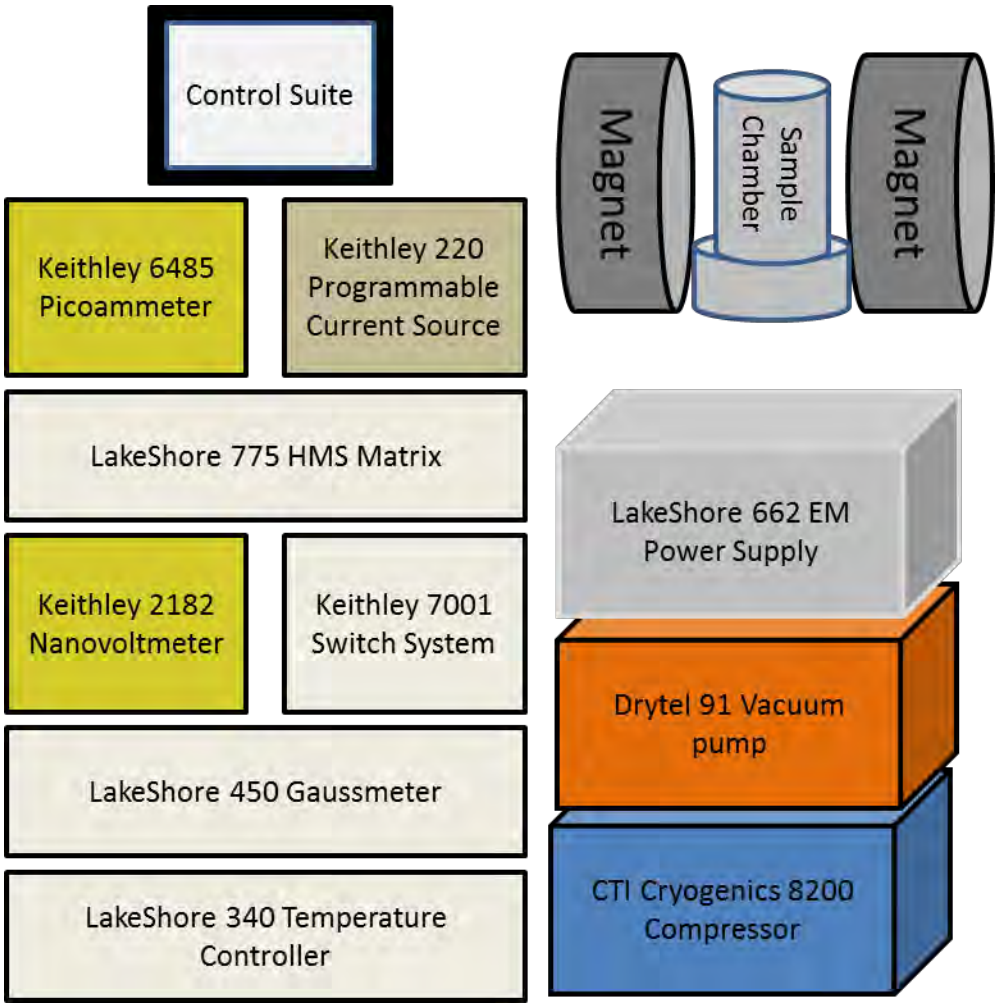

Appendix B

Responsivity Curve for the InGaAs Detector

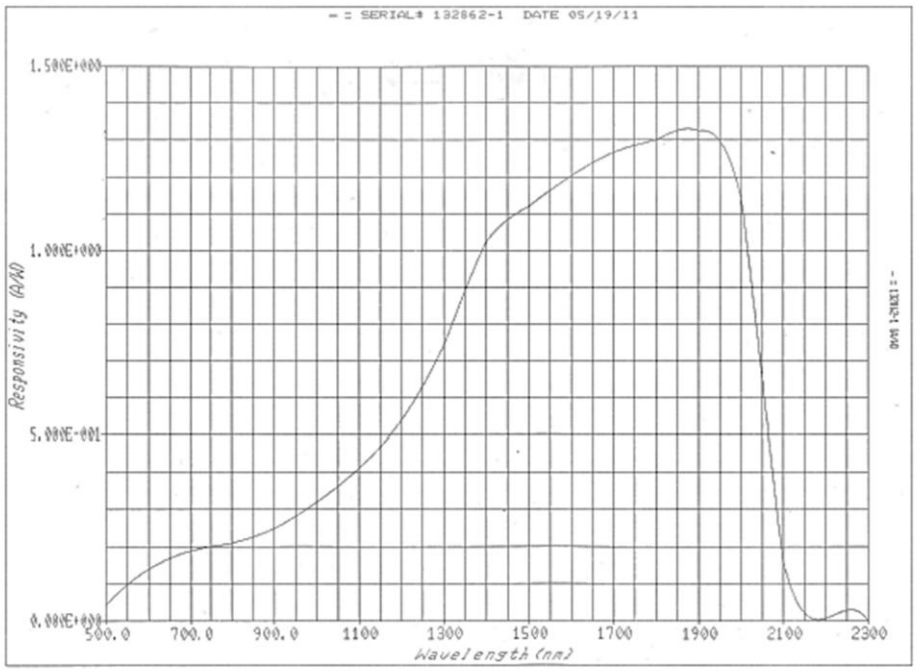

Figure 27. Responsivity curve for the InGaAs detector, provided by the manufacturer: Teledyne Judson Technologies©.

Appendix C

Response Curves for InGaAs and Ge Detectors*

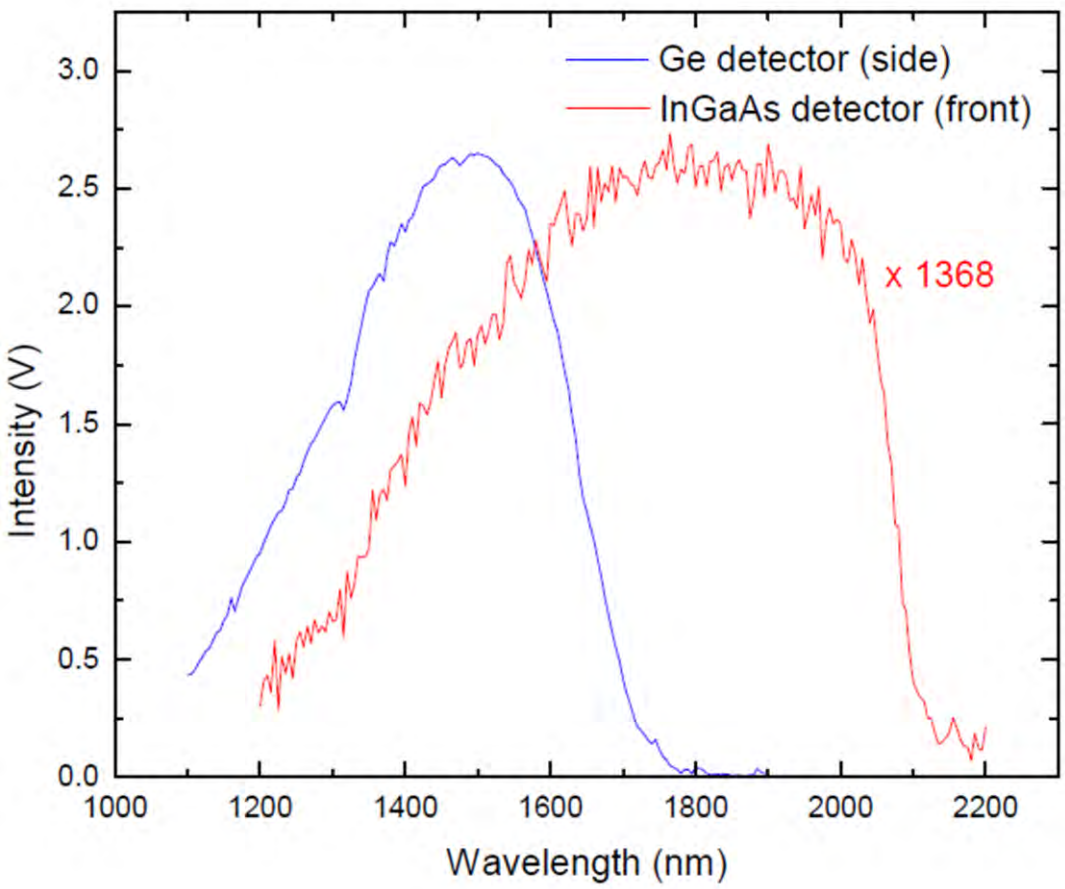

Figure 28. Response curves measured with the InGaAs and Ge Detectors used in photoluminescence. The Ge detector is 1368 times more sensitive at its peak responsivity when compared to the peak responsivity of the InGaAs Detector*.

*Data by T. Harris, PhD student at AFIT.

Appendix D

Hall Effect Measurement for Magnetic Field Correction

- **Resistivity**

Let B_S = sample field and B_P = field at magnetic pole.

$$R_{HS}^{real} = \frac{\Delta R_{13,24}}{B_S}$$

$$\Delta R_{13,24}^{real} = \left[R_{13,24}\right]_{B_S=0} - \left[R_{13,24}\right]_{B=B_S} \leftarrow \text{depends on B - field}$$

$$R_{HS}^{real} = \frac{\Delta R_{13,24}}{B_S} \times \frac{B_P}{B_P} = \left(\frac{B_P}{B_S}\right)\frac{\Delta R_{13,24}^{real}}{B_P} = \left(\frac{B_P}{B_S}\right) R_{HS}^{\text{computercalculated}}$$

Let r = real and cc = computer calculated.

(1) $\boxed{R_{HS}^{r} = \left(\frac{B_P}{B_S}\right) R_{HS}^{cc}}$ real accurate value to be obtained.

$$R_{HS}^{cc} = \frac{\Delta R_{13,24}}{B_P} \leftarrow \text{depends on applied B field}$$

- **Hall Mobility**

$$\mu_H^{real} = \frac{R_{HS}^{real}}{\rho_S} = \left(\frac{B_P}{B_S}\right)\frac{R_{HS}^{cc}}{\rho_S} = \left(\frac{B_P}{B_S}\right)\mu_S^{cc}$$

(2) $\boxed{\mu_H^{r} = \left(\frac{B_P}{B_S}\right)\mu_S^{cc}}$

- **Carrier concentration**

$$n_S^{real} = \frac{1}{eR_{HS}^{real}} = \frac{1}{e\left(\frac{B_P}{B_S}\right)R_{HS}^{cc}} = \left(\frac{B_S}{B_P}\right)\frac{1}{e\,R_{HS}^{cc}} = \left(\frac{B_S}{B_P}\right)n_S^{cc}$$

(3) $\boxed{n_S^{real} = \left(\frac{B_S}{B_P}\right) n_S^{cc}}$

At two different fields: B_{P1}, B_{P2}, B_{S1}, B_{S2}

$$R_{HS}^{r,1} = \frac{\Delta R^{r,1}}{B_{S1}} \text{ and } R_{HS}^{r,2} = \frac{\Delta R^{r,2}}{B_{S2}}$$

$$\Delta R^{r,1} = \left[R_{13,24}\right]_{B_S=0} - \left[R_{13,24}\right]_{B=B_{S1}} \text{ and } \Delta R^{r,2} = \left[R_{13,24}\right]_{B_S=0} - \left[R_{13,24}\right]_{B=B_{S2}}$$

$$R_{HS}^{r,1} = \left(\frac{B_{P1}}{B_{S1}}\right) R_{HS}^{cc1} \qquad R_{HS}^{r,2} = \left(\frac{B_{P2}}{B_{S2}}\right) R_{HS}^{cc2}$$

$$\mu_H^{r,1} = \left(\frac{B_{P1}}{B_{S1}}\right) \mu_H^{cc1} \qquad \mu_H^{r,2} = \left(\frac{B_{P2}}{B_{S2}}\right) \mu_H^{cc2}$$

$$n_S^{r,1} = \left(\frac{B_{S1}}{B_{P1}}\right) n_S^{cc1} \qquad n_S^{r,2} = \left(\frac{B_{S2}}{B_{P2}}\right) n_S^{cc2}$$

We must have $\boxed{\mu_H^{r,1} = \mu_H^{r,2} \quad \text{and} \quad n_S^{r,1} = n_S^{r,2}}$

Then $\left(\frac{B_{P1}}{B_{S1}}\right) \mu_H^{cc1} = \left(\frac{B_{P2}}{B_{S2}}\right) \mu_H^{cc2}$ or $\left(\frac{B_{S1}}{B_{P1}}\right) n_S^{cc1} = \left(\frac{B_{S2}}{B_{P2}}\right) n_S^{cc2}$

If $\left(\frac{B_{P1}}{B_{S1}}\right) = \left(\frac{B_{P2}}{B_{S2}}\right)$, then $\mu_H^{cc1} = \mu_H^{cc2}$ or $n_S^{cc1} = n_S^{cc2}$

Also, $\mu_H^{r,1} = \frac{R_{HS}^{r,1}}{\rho_S}$ and $\mu_H^{r,2} = \frac{R_{HS}^{r,2}}{\rho_S}$, then $\left(\frac{B_{P1}}{B_{S1}}\right) R_{HS}^{cc1} = \left(\frac{B_{P2}}{B_{S2}}\right) R_{HS}^{cc2}$

If $\left(\frac{B_{P1}}{B_{S1}}\right) = \left(\frac{B_{P2}}{B_{S2}}\right)$, then $R_{HS}^{cc1} = R_{HS}^{cc2}$ that is $\frac{\Delta R^{r,1}}{B_{P1}} = \frac{\Delta R^{r,2}}{B_{P2}}$

Therefore, $\boxed{R_{HS}^{r,1} = R_{HS}^{r,2}}$

Appendix E

Additional Experiments

G.1 Spectroscopic Ellipsometry

Spectroscopic ellipsometry experiments were performed at Air Force Research Laboratory's Materials Directorate. Spectroscopic ellipsometry measures the change in polarization state of light reflected from (or transmitted through) a surface. Specifically Ψ and Δ are measured and are related to the reflected polarization by

$$\frac{R_p}{R_s} = \tan(\Psi)\, e^{i\Delta}, \tag{E.1}$$

where $\tan(\Psi)$ is the amplitude of the ratio of reflection from the p and s waves and Δ is the phase shift. Using the Fresnel equations along with the values from equation E.1, the real part of the index of refraction, n, the imaginary part of the index of refraction, κ, and the real and imaginary dielectric constants, ϵ_1, and ϵ_2 may be calculated. The apparatus used was a J.A. Woollam Co Inc. V-VASE. All 5 *p*-SiGeSn samples were measured using samples of approximately 5 mm × 5 mm. The measurement range and step size were 1.00 eV to 0.564 eV and 0.001 eV respectively. Three measurements of each sample were taken at angles 65°, 70° and 75°.

Due to the samples' small sizes and the proximity of the *p*-$Si_{0.08}Ge_{0.90}Sn_{0.02}$ band edge to the *p*-Ge band edge, no critical points corresponding to the epilayer could be resolved in the spectrums of *p*-$Si_{0.08}Ge_{0.90}Sn_{0.02}$/*p*-Ge. The *p*-$Si_{0.112}Ge_{0.86}Sn_{0.028}$/*n*-Si did show one possible critical points at 75°, corresponding to 0.85 eV as shown in figure 29. Further analysis via a multilayer model needs to be done to verify this critical point.

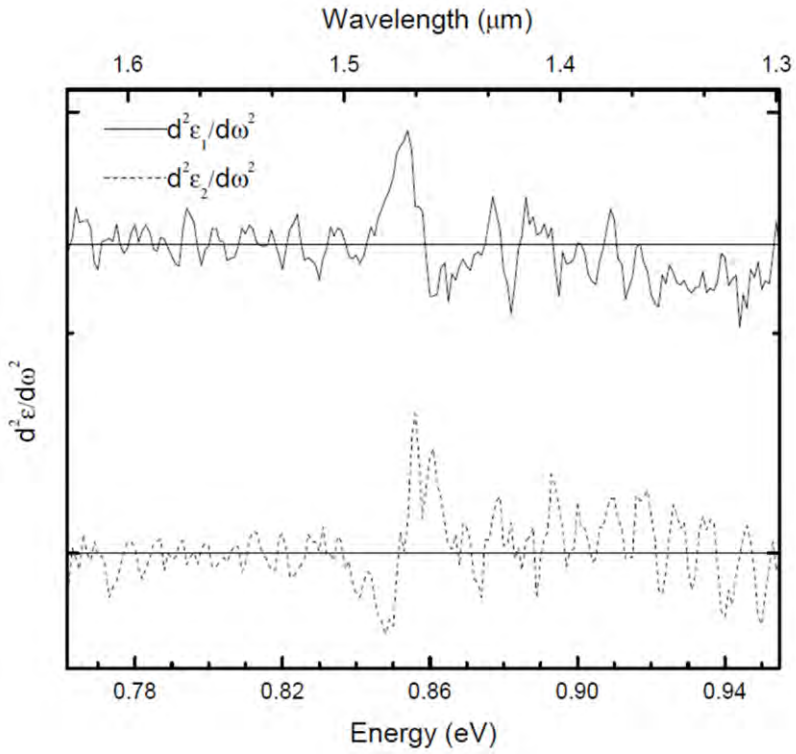

Figure 29. Second derivative of the real and imaginary dielectric constants, ϵ_1 and ϵ_2 (dashed,) as a function of energy. The measurements are displaced for clarity. One critical point is observed at 0.85 eV.

G.2 Franz Keldysh Effect

Using a multimeter and a 12 V power supply, a measurement of transmission was performed on the 750 nm thick *p*-$Si_{0.08}Ge_{0.90}Sn_{0.02}$/*p*-Ge sample with ohmic contacts on the FTIR as shown in figure 30.

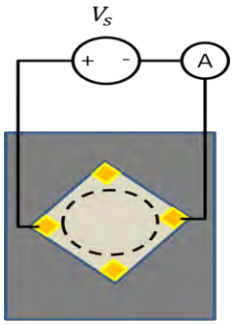

Figure 30. Transmission with a parallel to surface electric field experiment. The dashed circle indicates the portal through which transmission was measured by the FTIR.

The purpose of the experiment was to examine the shifting of *p*-Ge substrate band edge. This will determine if interrogation of the *p*-$Si_{0.08}Ge_{0.90}Sn_{0.02}$ epilayer band edge might be possible with an applied electric field. From Fox [20], the epilayer band edge may be observable due to the lowering of the band edge with increasing electric field, *F*, by

$$\alpha \sim e^{-\frac{4\sqrt{2m^*}}{3|q|\hbar F}(E_g-\hbar\omega)^{\frac{3}{2}}}, \qquad \text{(G.2)}$$

where $\hbar$ is Plank's constant divided by 2π, q is the magnitude of charge of the electron, E_g is the bandgap energy of the material, m^* is the effective mass, and $\hbar\omega$ is the incident energy. The band edge of the epilayer was not observed, however changes in valence band transitions were measured as shown in figure 31. This could lead to an interesting future study.

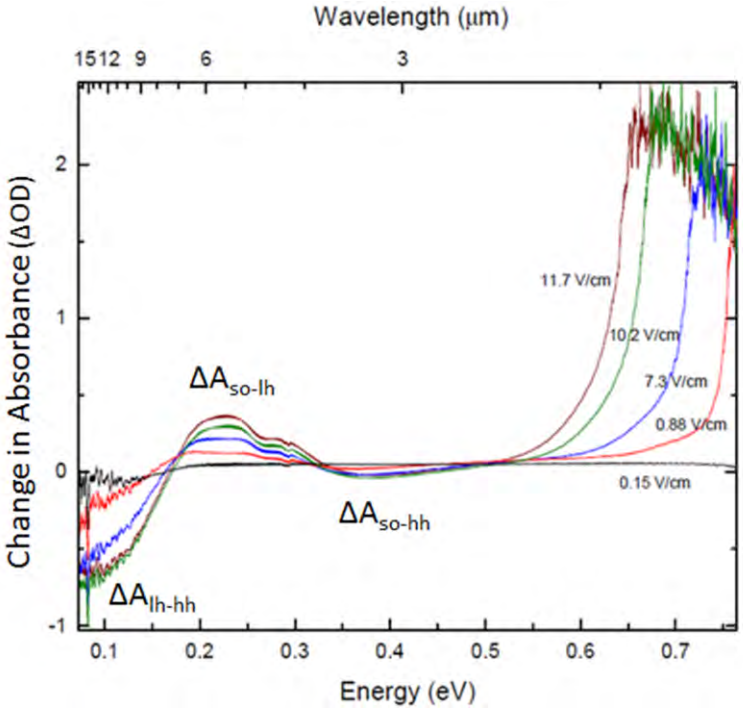

Figure 31. Change in absorbance as a function of energy with a parallel field applied to the epilayer of the 750 nm thick *p*-$Si_{0.08}Ge_{0.90}Sn_{0.02}$/*p*-Ge. An applied electric field of 0.15, 0.88. 7.3, 10.2, and 11.7 V/cm is shown. The so→hh and lh→hh showed decreased absorption while the so→lh exhibited increased absorption.

Appendix F

Carrier Concentration and Mobility for the *p*-$Si_{0.112}Ge_{0.86}Sn_{0.028}$/*n*-Si Sample

The carrier concentration and mobility for the *p*-$Si_{0.112}Ge_{0.86}Sn_{0.028}$/*n*-Si are shown here for reference. These data were measured by Dr. M. Ryu at the Air Force Institute of Technology. This sample differs from the four *p*-$Si_{0.08}Ge_{0.90}Sn_{0.02}$/*p*-Ge samples in that a type conversion occurs at 395 K. This is due to the larger electron mobility compared to the hole mobility in the intrinsic regime as shown in figure 32. Additionally, the onset of the intrinsic regime is closer to room temperature. Around 700 K, several data points appear to diverge from the trend below that temperature. This is due to poor thermal contact of the sample and the hot finger.

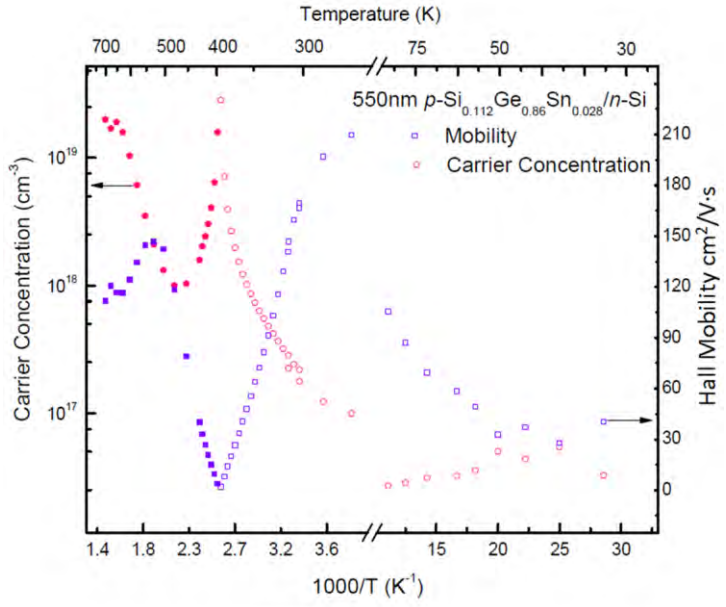

Figure 32. The carrier concentration and hall mobility as a function of inverse temperature for the *p*-$Si_{0.112}Ge_{0.86}Sn_{0.028}$/*n*-Si sample, corresponding to the left and right axes, respectively. Type conversion occurs at 395 K due to the larger electron mobility than hole mobility in the high temperature regime.

Bibliography

1. C. Schow, F. Doany and J. Kash, "Get On the Optical Bus," Spectrum, IEEE 47 (9), 32-56 (2010).

2. Intel©, "Intel Milestone Confirms Light Beams Can Replace Electronic Signals for Future Computers," 2011 (June 09, 2011), (2010).

3. M. Bauer et al., "Ge-Sn Semiconductors for Band-Gap and Lattice Engineering," Appl.Phys.Lett. 81 (16), 2992-2994 (2002).

4. J. Mathews et al., "Extended Performance GeSn/Si(100) *p-i-n* Photodetectors for Full Spectral Range Telecommunication Applications," Applied Physics Letters 95 (13), 133506-133506-3 (2009).

5. Y. K. Yeo, "Investigation of Optical and Electrical Properties of GeSn and SiGeSn Material Systems for the Si-Based Light Emitter Applications," (2010).

6. J. Tolle et al., "Compliant Tin-Based Buffers for the Growth of Defect-Free Strained Heterostructures on Silicon," Applied Physics 88 (25), 252112 (2006).

7. J. Mathews et al., "Direct-Gap Photoluminescence with Tunable Emission Wavelength in $Ge_{1-y}Sn_y$ Alloys on Silicon," Appl.Phys.Lett. 97 (22), 221912 (2010).

8. M. R. Bauer et al., "SnGe Superstructure Materials for Si-based Infrared Optoelectronics," Appl.Phys.Lett. 83 (17), 3489-3491 (2003).

9. J. Kouvetakis, in LEOS Annual Meeting Conference Proceedings, 2009. LEOS '09. IEEE, (2009), pp. 211-212.

10. J. Singleton, Band Theory and Electronic Properties of Solids, (Oxford University Press, 2001), pp. 240.

11. B. Sapoval and C.L. Hermann, Physics of Semiconductors, (Springer-Verlag, New York, 1995).

12. G. Leman, Annales de Physique 7, 505 (1962).

13. C. F. Klingshirn, Semiconductor Optics, 3rd ed. (Springer Science, 2007), pp. 809.

14. P. T. Landsberg, Recombination in Semiconductors, (Cambridge University Press, 1991), pp. 595.

15. J. Pankove, Optical Processes in Semiconductors, (Courier Dover Publications, 1971), pp. 422.

16. J. Wagner and L. Vina, "Radiative Recombination in Heavily Doped *p*-type Germanium," Phys.Rev.B 30 (12), 7030-7036 (1984).

17. A. H. Kahn, "Theory of the Infrared Absorption of Carriers in Germanium and Silicon," Phys.Rev. 97 (6), 1647-1652 (1955).

18. P. K. Basu, Theory of Optical Processes in Semiconductors: Bulk and Microstructures, (Oxford University Press, 2003), pp. 464.

19. S. Chichibu *et al.*, "Urbach--Martienssen tails in a wurtzite GaN epilayer," Appl. Phys. Lett (70), 3440 (1997).

20. A. M. Fox, Optical Properties of Solids, (Oxford University Press, 2010), pp. 396.

21. D. Look and R. Molnar, "Degenerate layer at GaN/sapphire interface: Influence on Hall-effect measurements," Appl. Phys. Lett. (70), 3377 (1997).

22. W. R. Thurber, "The Hall Effect," 2011, (2011).

23. J. P. McKelvey, Solid State and Semiconductor Physics, (Kreiger Publishing, 1982), pp. 512.

24. C. Dale, "Alloy scattering Limitation on the Mobility of Holes in *p*-type $GaAs_{1-x}Sb_x$," Thesis, (1999).

25. J. Kouvetakis, "PPT: Growth and Properties of Si-Ge-Sn Materials," Presentation given at the Air Force Institute of Technology, (2010).

26. Y-Y Fang et al., "Practical B and P doping via $Si_xSn_yGe_{1-x-y-z}M_z$ Quaternaries Lattice Matched to Ge: Structural, Electrical, and Strain Behavior," Appl.Phys.Lett. 95 (8), 081113 (2009).

27. J. Kouvetakis et al., "Practical Materials Chemistry Approaches for Tuning Optical and Structural Properties of Group IV Semiconductors and Prototype Photonic Devices," Photonics Journal, IEEE 2 (6), 924-941 (2010).

28. J. Xie et al., "Direct Integration of Active $Ge_{1-x}(Si_4Sn)_x$ Semiconductors on Si(100)," Appl.Phys.Lett. 95 (18), 181909 (2009).

29. R. Soref et al., "Advances in SiGeSn/Ge Technology," Group IV Semiconductor Nanostructures—2006, edited by Leonid Tsybeskov, David J.Lockwood, Christophe Delerue, Masakazu Ichikawa, and Anthony W. van Buuren , (2007).

30. S. H. Groves et al., "Interband Magnetoreflection of α-Sn," Journal of Physics and Chemistry of Solids 31 (9), 2031 (1970).

31. J. Liu et al., "Tensile-strained, *n*-type Ge as a Gain Medium for Monolithic Laser Integration on Si," Optical Express 15 (18), 11272 (2007).

32. W. C. Dash and R. Newman, "Intrinsic Optical Absorption in Single-Crystal Germanium and Silicon at 77 K and 300 K," Phys. Rev. (4), 1151 (1955).

33. M. Ryu et al., "Hall-Effect Studies on Lightly Boron Doped Direct Bandgap *p*-type GeSn Grown on *n*-Si Substrate," unpublished, (2012).

34. O. A. Golikova, B. Ya Moizhes and L. S. Stil'bans, "Germanium Hole Mobility," Sov. Phys. Solid State (English Transl.) 3, 2259 (1962).

REPORT DOCUMENTATION PAGE

Form Approved
OMB No. 074-0188

1. REPORT DATE *(DD-MM-YYYY)*	2. REPORT TYPE	3. DATES COVERED *(From – To)*
22-03-2012	Master's Thesis	March 2011 – March 2012

Electrical and Optical Characterization of Si-Ge-Sn

5a. CONTRACT NUMBER
5b. GRANT NUMBER
5c. PROGRAM ELEMENT NUMBER

6. AUTHOR(S)
Hamilton, Merle D., Captain, USAF

5d. PROJECT NUMBER
5e. TASK NUMBER
5f. WORK UNIT NUMBER

7. PERFORMING ORGANIZATION NAMES(S) AND ADDRESS(S)
Air Force Institute of Technology
Graduate School of Engineering and Management (AFIT/ENP)
2950 Hobson Way, Building 640
WPAFB OH 45433-7765

8. PERFORMING ORGANIZATION REPORT NUMBER
AFIT/APPLPHY/ENP/12-M06

9. SPONSORING/MONITORING AGENCY NAME(S) AND ADDRESS(ES)
Air Force Office of Scientific Research/RSE
875 N. Randolph St.
Arlington, VA 22203
Attn: Gernot Pomrenke, E-mail: gernot.pomrenke@afosr.af.mil
Comm: (703) 696-8426

10. SPONSOR/MONITOR'S ACRONYM(S)
AFOSR

11. SPONSOR/MONITOR'S REPORT NUMBER(S)

12. DISTRIBUTION/AVAILABILITY STATEMENT
APPROVED FOR PUBLIC RELEASE; DISTRIBUTION UNLIMITED.

13. SUPPLEMENTARY NOTES

14. ABSTRACT

The electrical characterization of boron-doped p-$Si_{0.08}Ge_{0.90}Sn_{0.02}$/$p$-Ge(100) and p-$Si_{0.112}Ge_{0.86}Sn_{0.028}$/$n$-Si(100) with various epilayer thicknesses was measured using the Hall effect. The room temperature sheet carrier concentration ranged from $1.21 \times 10^{13} - 1.32 \times 10^{16}$ cm^{-2}. The room temperature mobilities were measured to be between 166 and 717 cm^2/V·s, depending on sample composition. In the low temperature regime, the mobility was mainly affected by ionized impurity scattering. In the high temperature regime, the mobility was mainly affected by both alloy and lattice scattering. The acceptor activation energy was estimated to be 10.7 meV. The Hall data indicated that an interfacial layer between the epilayer and substrate participated in both carrier concentration and hall mobility measurements. From the results of infrared transmission measurements of the p-$Si_{0.08}Ge_{0.90}Sn_{0.02}$/$p$-Ge(100) at room temperature, an effective mass was estimated to be $m_{hh} = 0.30m$, $m_{lh} = 0.051m$, $m_{so} = 0.79m$, and $\Delta\epsilon = 0.30\ eV$, where $\Delta\epsilon$ is the splitting between heavy hole and split-off valence bands. The indirect and direct bandgap energy values for the p-$Si_{0.112}Ge_{0.86}Sn_{0.028}$/$n$-Si(100) were estimated to be 0.780 eV and 0.845 eV, respectively. The results of photoluminescence measured at 15 K, for the p-$Si_{0.08}Ge_{0.90}Sn_{0.02}$/$p$-Ge(100) sample with a 600 nm film thickness, revealed the onset of a luminescence peak at 0.885 eV.

15. SUBJECT TERMS
Si-Ge-Sn, Transmission, Hall Effect, Absorption, Photoluminescence, Mobility, Carrier Concentration, Conductivity, Resistivity, Interband, Valence Band, Effective Mass

16. SECURITY CLASSIFICATION OF:			17. LIMITATION OF ABSTRACT	18. NUMBER OF PAGES	19a. NAME OF RESPONSIBLE PERSON
a. REPORT	b. ABSTRACT	c. THIS PAGE			Dr. Yung Kee Yeo
U	U	U	UU	82	19b. TELEPHONE NUMBER *(Include area code)* (937) 255-6565, ext 4532 (yung.yeo@afit.edu)

Standard Form 298 (Rev. 8-98)
Prescribed by ANSI Std. Z39-18